Control of Upswept Afterbody Vortices Using Continuous and Pulsed Blowing

Richard Jackson[1], *Zhijin Wang*[2], *Ismet Gursul*[3]
Department of Mechanical Engineering, University of Bath
Bath BA2 7AY, United Kingdom

Abstract

An experimental study was performed in a water tunnel to evaluate the effects of continuous and pulsed blowing jets on the counter-rotating vortices generated by the afterbody of a slanted base cylinder. Drag reductions from continuous blowing through circular jets were found to vary significantly with direction and location, and approached 7% when blowing outboard from upstream locations on the upswept face. However, for all circular jets tested, the external power required was larger than the power saved due to the drag reduction. Jet vortices restricted shear layer development, leading to smaller afterbody vortex cores further from the surface. A high aspect ratio jet flap, ejecting nearly parallel to the freestream, achieved drag reductions close to 9%, equating to the net energy savings of almost 3% for the best case. Jet vortices shortened the shear layer, resulting in vortices with reduced circulation, which were displaced away from the upswept face. Pulsing the jet flap resulted in improved drag reductions and energy savings (up to around 6%) compared to the equivalent continuous blowing case at the same time-averaged jet momentum coefficient. Pulsed blowing caused an increase in vortex separation and meandering, while the circulation was reduced by up to 10% of that for continuous blowing.

[1] Research Associate
[2] Senior Lecturer
[3] Professor, Associate Fellow of AIAA

Nomenclature

A_j	=	cross-sectional area of jet
b	=	spanwise separation of vortex centroids
C_D	=	drag coefficient
C_μ	=	jet momentum coefficient, $\rho A_j U_j^2 / 0.5 \rho U_\infty^2 S$
$\overline{C}_\mu$	=	time-averaged jet momentum coefficient
c	=	chord length of upswept face
D	=	diameter of fuselage
f	=	jet pulsing frequency
h	=	vertical distance of vortex centroid from upswept surface
L	=	length of afterbody
$\dot{m}_j$	=	mass flow of jet, $\rho A_j U_j$
P	=	drag power, $C_D 0.5 \rho U_\infty^3 S$
P_{in}	=	jet power, $0.5 \dot{m}_j U_j^2$
P_{net}	=	net power savings
Re_D	=	Reynolds number based on diameter, $\rho U_\infty D / \mu$
S	=	cross-sectional area of fuselage
T	=	time period of pulsed jet
U_j	=	jet velocity
U_∞	=	freestream velocity
V_{rms}	=	root-mean-square of crossflow velocity
x	=	streamwise distance
x'	=	local co-ordinate along upswept face
x_j	=	streamwise jet location

y	=	normal distance
z	=	spanwise distance
z_j	=	spanwise jet location
α_j	=	jet incidence angle
β_j	=	jet yaw angle
Γ	=	circulation
μ	=	viscosity
ρ	=	density
φ	=	upsweep angle
ω	=	vorticity

1 Introduction

To allow for their rear-loading capability, many military transport aircraft are designed with a steep upsweep angle. The Lockheed Martin C-130 'Hercules' has an upsweep angle of $\varphi = 28°$, compared with the shallower upsweep angles of civilian passenger aircraft in the range of $12° < \varphi < 16°$. Previous studies have used simplified fuselage models to demonstrate that an aircraft with a larger upsweep angle has an inherently larger drag coefficient, indicating that this problem is more pertinent to cargo aircraft [1, 2]. It has also been suggested that the afterbody drag may contribute towards a significant portion of the total aircraft drag [3].

It is known that when the upsweep angle is less than a critical value (between 45° and 50°), a counter-rotating vortex pair develops [4-7]. There is evidence to suggest that the vortex circulation is roughly proportional to the upsweep angle [7]. The low pressure

on the upswept face causes a reduction in lift, in addition to an increase in drag [2, 8]. Furthermore, the vortices are capable of disrupting the initial path of payloads and paratroopers during airdrop missions.

Several passive flow control solutions have demonstrated reductions in drag coefficient through controlling the afterbody vortices. One of the earliest examples dates back to the 1960s, where vertical strakes were mounted close to the edge of the upsweep of the Short Belfast [9]. The aim was to reduce inflow to the vortex pair, thereby delaying their formation. Results indicated drag reductions of up to 7%. However, it was identified that up to half of the potential drag reduction was lost through the parasitic drag of the strakes themselves. These strakes can also limit airdrop capabilities. Other passive methods have included arrays of co-rotating and counter-rotating vortex generators. These were either mounted on the fuselage underside upstream of the upsweep apex, or along the edge of the fuselage breakline extending aft towards the tail [10-12]. The vortices produced by the vortex generators were designed to delay separation and weaken the afterbody vortices. The drag coefficient was reduced by up to 6% in some cases, with a strong dependency on geometry and arrangement. A different approach was used for an axisymmetric cylinder with a slanted base [13]. Small flaps/spoilers placed perpendicularly on the slanted surface displaced the afterbody vortices away from the surface, resulting in a drag reduction worth around 5%. It is known that vortex displacement is one of the flow control strategies to reduce the vortex-induced force associated with tip/edge vortices [14].

There is limited evidence of the efficacy of active flow control techniques when applied to the tip/edge vortices as external power is required. Continuous blowing outboard via

a pair of circular jets was shown to be successful at weakening the afterbody vortices [6, 15]. Other examples of vortex modification using active flow control include turbulence ingestion to diffuse wing tip vortices in the near-wake [16, 17]. The degree of control was shown to be highly dependent on blowing location, direction and jet momentum coefficient C_μ. Spanwise and surface-normal wing tip blowing can also result in the diffusion of the wing tip vortex, and involves the interaction of jet-generated vortices with the main vortex [18, 19]. In addition, spanwise blowing can deflect the tip vortex to a position further from the wing surface [20]. Like upswept aircraft afterbodies, the rear slant on Ahmed bodies induces flow separation and the formation of a counter-rotating vortex pair. Significant drag reductions worth over 10% have been demonstrated on Ahmed bodies using continuous and pulsed blowing from slot jets and microjet arrays on the slant surface [21-23]. These examples were shown to be effective at controlling flow separation, increasing the surface pressure on the slant and weakening the vortex pair.

Although active flow control can be effective for drag reduction, it requires external power. Whether there are net energy savings or not is often not reported. The aim of this study was to evaluate the energy savings for a slanted base cylinder by using continuous and pulsed blowing to interfere with the formation of the afterbody vortices. Both circular jets and high aspect ratio slot blowing were investigated at various locations and directions. The flow field measurements using Particle Image Velocimetry (PIV) and direct drag force measurements were carried out. These data together with the calculated energy savings are presented for various blowing configurations.

2 Experimental Methods

2.1 Experimental Set-up

Experiments were performed in a free-surface, closed-loop water tunnel. The tunnel has a test section of width 381 mm and height 508 mm where flow can reach a maximum freestream velocity of 0.5 m/s. The turbulence intensity has previously been measured using Laser Doppler Velocimetry to be less than 0.5% across the flow velocity range. The Reynolds number of the flow based on fuselage diameter was fixed at Re_D = 20,000, resulting in a freestream velocity of around U_∞ = 0.25 m/s. The estimated uncertainty in setting the freestream velocity is ±2%. An overview of the experimental setup is presented in Fig. 1.

The model that generated the flow field of interest is a slanted-base axisymmetric cylinder, used as an approximation of an upswept fuselage. The model has an ellipsoidal nose and a flat upswept face at an angle of $\varphi = 28°$, which is within the range of many military transport aircraft. The diameter of the model is D = 89 mm and the afterbody fineness ratio is L/D = 1.88. An overview of the model parameters is outlined in Fig. 2(a). The energy for the blowing jets was provided by a pressurized air supply in a large container with water, as sketched in Fig. 2(b). The water delivery system fed into a plenum chamber, which was located behind the upswept face, and served as a settling chamber before ejecting water out through circular holes or high aspect ratio slots. The jet momentum coefficient, C_μ, was controlled using a valve and flowmeter upstream.

2.2 Blowing Configurations

Figures 3 and 4 illustrate the blowing configurations tested with circular jets and high

aspect ratio jets respectively. A pair of circular jets, of 1 mm diameter, were moulded in discs to allow for simple manual control of the jet direction. The jets were positioned on the upswept surface and were symmetric about the $z = 0$ plane as demonstrated in Fig. 3a for one example jet position. The chordwise (x') and spanwise (z_j) jet locations were varied, in addition to the jet incidence (α_j) and yaw angles (β_j). The uncertainty in setting the jet angle was estimated to be ±2°. The tested chordwise jet locations were $x'_j/c = 0.12$, 0.2, 0.3 and 0.4. The spanwise spacing between adjacent stations was $\Delta z =$ 5 mm, equivalent to $\Delta z_j/D = 0.056$. The jet locations are shown in Fig. 3b, with the majority outboard of the vortex core (shown by the dashed trajectory), to increase the likelihood of disrupting vortex formation. Preliminary flow visualisation results indicated that blowing at locations further downstream than $x'_j/c = 0.4$ had little effect upon the afterbody vortices. The definition of the jet incidence and yaw angles is depicted in Fig. 3c. The jet incidence angle was tested at $\alpha_j = 30°$ and $\alpha_j = 90°$. The lower incidence angle was limited by the thickness of the discs (3 mm) through which the jets exited. The total jet momentum coefficient was fixed for all cases at $C_\mu = 0.02$ (or $C_\mu = 0.01$ per jet). The jet velocity was approximately $U_j = 1.6$ m/s, giving a velocity ratio of around $U_j/U_\infty = 6.4$.

Three slot jet configurations were tested: surface-normal from the upswept face, spanwise blowing away from the upsweep edge, and blowing from near the upsweep apex close to the direction of the freestream (see Figure 4). For surface-normal blowing, a pair of slot jets of width 0.5 mm were positioned on the upswept face, close to the edge of the upsweep, and symmetric about the $z = 0$ plane. The jets exited perpendicular to the surface, as shown in Fig. 4a. The position of the slots for one example jet location is outlined in Fig. 4b.

For spanwise blowing, a pair of slot jets of width 0.5 mm were positioned on either side of the afterbody, parallel to the upsweep edge, and offset by 2.5 mm. The aim of the jet was to disrupt the shear layer, similar to previous wing tip blowing studies [18]. The location of one of the slots and the direction of the jets are shown in Fig. 4c and Fig. 4d, respectively. For this example, they extended from x_j/L = 0.1 to x_j/L = 0.25, each with a length of L = 28.5 mm. The velocity ratio of this case was U_j/U_∞ = 1.6.

A jet flap was positioned close to the upstream apex of the slant at x'_j/c = 0.07, with the aim of minimizing flow separation on the upswept face, as previously shown on other bodies with slanted bases [21]. The jet incidence angle was varied, which is defined in Fig. 4e. The slot spanned 30 mm and had a width of 0.5 mm. Its location relative to the baseline vortex trajectory is shown in Fig. 4f. The velocity ratio of the jet flap was U_j/U_∞ = 2.1.

For the pulsed jet experiments, the jet flap design is the same as that used in the continuous blowing experiments shown in Fig. 4e and Fig. 4f, and angled at α_j = 30°. An Alicat liquid flow controller (model LCR-1SLPM-D) replaced the variable area flowmeter used in previous studies, to enable the generation of a periodic jet and ensure more accurate measurement of the flow rate. The controller initially laminarizes the flow through a series of flow elements. The pressure drop across the flow meter is then measured internally, before the flow rate is calculated using the Hagen-Poiseuille equation. The controller was accessed remotely from a PC via a serial link, from which a demand was sent and data acquired using a LabVIEW program. Data was transferred between the PC and the flow controller at approximately 40 measurement points per

second. The flow controller was synchronized with the PIV and force measurement systems to enable the collection of phase-locked data for a given point along the pulsed jet cycle. Frequencies higher than $fD/U_\infty = 0.82$ could not be achieved due to the limited response time between the PID controller and flow meter.

2.3 Force Measurements

A Futek 'S Beam' load cell with a capacity of 0.5 N was used to measure the drag force. One end was fixed in-situ, with the free end under tension from the drag force acting on the model. As the weight-to-drag ratio of the model was significant, its weight was supported by a carriage mounted to two parallel rails, each of which passed through a set of air bearings to ensure frictionless displacement of the load cell. The rails were positioned parallel to the freestream flow. Any moments were absorbed by the bearings. The data for the baseline and flow control cases were collected for 90 seconds at a sampling rate of 500 Hz. An end plate was placed just beneath the free-surface in order to prevent free-surface oscillations being transmitted to the load cell.

The drag change is defined as $\Delta C_D = C_{D1} - C_{D0}$ (where subscripts 0 and 1 are the baseline and flow control conditions, respectively). Hence, ΔC_D is negative for drag reductions. The power saved due to drag reduction can be defined as:

$$\Delta P = \Delta C_D \frac{1}{2} \rho U_\infty^3 S. \quad (1)$$

Assuming that the flow in the plenum chamber is at rest and that there is negligible change in potential and pressure energy, then the power supplied to the jet is:

$$P_{in} = \frac{1}{2} \dot{m}_j U_j^2 \quad (2)$$

Here we considered the power supplied to the jet and the energy balance for the fluid only. Any additional external mechanical or electrical power depends on the actuation system, and its optimization is beyond the scope of this paper. The energy balance is then considered by the net power savings, $P_{net}=\Delta P+P_{in}$. If this is normalized by $P_{D0} = C_{D0}0.5\rho U_\infty{}^3 S$, then:

$$\frac{P_{net}}{P_{D0}} = \frac{\Delta P + P_{in}}{P_{D0}} = \frac{\Delta C_D}{C_{D0}} + \frac{C_\mu}{C_{D0}} \frac{U_j}{2U_\infty}, \tag{3}$$

where $C_\mu = \dot{m}_j U_j / 0.5\rho U_\infty{}^2 S$. Therefore, the net energy balance is dependent on the drag reduction, jet momentum coefficient and velocity ratio. The uncertainty in the drag reduction, $\Delta C_D/C_{D0}$, was estimated to be ±0.5%, using the Constant Odds Combination method introduced by Moffat [24]. Similarly, the uncertainty in net energy savings, P_{net}/P_{D0}, was estimated to be ±1.0%.

2.4 PIV Measurements

Crossflow PIV measurements were carried out at five equidistant stations along the afterbody length (x/L = 0.2, 0.4, 0.6, 0.8 and 1.0). A 4MP 12-bit digital CCD camera captured the images at a rate of 15 Hz and this was positioned downstream of the tunnel, facing the afterbody. Velocity data was also collected within the z = 0 plane, with the laser positioned underneath the test section, and the camera from the side. Spherical glass particles with diameters of 8 μm to 12 μm were used to seed the flow, and these were illuminated using a 120 mJ dual-head Nd:YAG laser which generated a sheet of light approximately 1 mm thick. The operation of the laser and camera was controlled using a TSI Model 610034 synchronizer. Time-averaged results were processed from

500 pairs of images collected at each station. The processor used the Hart correlation algorithm with an interrogation window of 32 x 32 pixels and 50% overlap, which resulted in a vector resolution of less than 1% of the model diameter.

3 Results

3.1 Circular jets

The effect of the spanwise and streamwise location of the pair of circular jets was first tested for three different jet directions: $\alpha_j = 30°$, $\beta_j = 0°$ (outboard blowing), $\alpha_j = 30°$, $\beta_j = 90°$ (streamwise blowing) and $\alpha_j = 90°$ (surface-normal blowing). Outboard blowing has previously demonstrated diffusion of the afterbody vortex pair [6], while there is evidence that streamwise and surface-normal blowing can attenuate wing tip vortices [16-19]. Figure 5 demonstrates the influence of blowing location and the three jet directions on the reduction in drag coefficient as a percentage of the baseline. Outboard blowing (Fig. 5a) is most effective at the furthest inboard and upstream location, where a drag reduction of $\Delta C_D/C_{D0} = -4.8\%$ is achieved. The benefit reduces with further aft and further outboard jet locations. Blowing in the streamwise direction (Fig. 5b) is more beneficial at further outboard locations, but is less dependent on streamwise position. Significant reductions of between $\Delta C_D/C_{D0} = -5\%$ and $\Delta C_D/C_{D0} = -7\%$ are demonstrated at several locations. Jets blowing perpendicular to the surface (Fig. 5c) are shown to be the least effective at reducing the drag, with a maximum reduction of $\Delta C_D/C_{D0} = -2.7\%$ and with little variation across the test region.

A study into the effect of β_j was undertaken to identify if there are any jet yaw angles at which further reductions can be achieved. For these experiments, the jet pitch angle was fixed at $\alpha_j = 30°$. Figure 6 demonstrates the effect of β_j at the designated locations

A, B, C and D. These locations are shown on the small inset figure. The drag reductions at these stations are compared with the theoretical component of jet thrust in the x-direction to reveal improvements due to favorable jet/vortex interactions (Fig. 6a). Blowing outboard from location B adds some benefit on to the theoretical jet thrust component. The greatest drag reduction occurs at βj = 30°, where the total drag reduction is $\Delta C_D/C_{D0}$ = -6.7%. At the outboard and downstream stations of locations A and C, the benefits of blowing outboard are no longer achieved. The drag reduction matches closely with the theoretical model, except in the region of upstream blowing, where the overall improvement due to upstream blowing is negligible for all stations. The corresponding net energy is calculated from Equation 3 and is shown in Fig. 6b. This is compared against the net energy if the drag reduction was purely from the theoretical thrust. The net energy increase ranges from P_{net}/P_{D0} = 9% to P_{net}/P_{D0} = 17% across the test cases. One reason for the significant energy increase is the high jet velocity. Again, the overall trend of the data is similar to that of the theoretical prediction.

As the variations of the drag reduction and net power follow the theoretical predictions, we conclude that the direction of the momentum flux of the jet itself is the dominant factor in the drag reduction, while the net power is more affected by the jet velocity ratio for a fixed momentum coefficient. Figure 6 explains why some directions (such as closer to the streamwise direction) are better than the others (such as closer to the upstream direction). On the other hand, the *additional* benefit of the jet is significant for upstream blowing, which can be attributed to the beneficial jet/vortex interactions. To understand this better, Figure 7 presents the time-averaged vorticity field for an upstream blowing case into the vortex cores, with the direction of the jets opposing the

vortex trajectories (location D, α_j = 30°, β_j = 247°). For this blowing configuration, Figure 6(a) indicates a drag increase. At x/L = 0.2 (Fig. 7a), the shear layer is greatly weakened, before the vortices form with smaller cores (Fig. 7b and Fig. 7c). The vortices are much more diffuse at further downstream locations of x/L = 0.8 and x/L = 1.0, showing symptoms of vortex breakdown (Fig. 7d and Fig. 7e). With reduced swirl velocity, a diffused vortex is likely to generate less force on the solid surface, therefore less drag. This drag reduction is offset by the direction of the momentum flux of the jet blowing upstream. On the other hand, a potential advantage of upstream blowing is to dissipate the vorticity, which may alleviate any deviations in the trajectory of payloads during airdrop missions caused by the swirling flow in the afterbody vortices.

The time-averaged vorticity field of an outboard blowing case at location B, α_j = 30°, β_j = 0°, is compared against the baseline in Fig. 8. This case resulted in drag reductions worth almost 5% (Fig. 6a), which is nearly 4% higher than the theoretical drag reduction. The jet interaction with the afterbody flow field generates a pair of counter-rotating vortices, which initially prevent the shear layer from developing too far inboard, as shown at x/L = 0.2 (Fig. 8a). The developing vortices at x/L = 0.4 are restricted to positions further outboard and with smaller vortex cores (Fig. 8b). This is also the case at x/L = 0.6 and x/L = 0.8 (Fig. 8c and Fig. 8d). Smaller vortices are likely to generate less drag force on the surface. The resultant vortices at the trailing edge appear more diffuse (Fig. 8e).

The root-mean-square (RMS) crossflow velocity of the baseline flow field is compared against the outboard blowing (β_j = 0°, location B, α_j = 30°) and upstream blowing (β_j = 247°, location D, α_j = 30°) cases in Fig. 9 for the three furthest upstream stations. The

turbulence in the baseline case arises mainly within the shear layer at x/L = 0.4 and x/L = 0.6. Very little turbulence is observed in the afterbody vortex cores, suggesting low meandering amplitudes. For outboard blowing, a concentrated region of turbulence at x/L = 0.2 is likely to be due to the interaction of the jet vortices with the afterbody flow field. Further downstream, the RMS velocity within the afterbody vortex shear layer is reduced. The unsteadiness caused by the jet vortices is still evidenced at x/L = 0.4 and x/L = 0.6, inboard of the afterbody vortex cores, likely to be a footprint of the jet vortices. Upstream blowing generates a much more intense region of turbulence at x/L = 0.4, which leads to the dissipation of vorticity further downstream (Fig. 7) due to vortex breakdown. Although outboard blowing was shown to reduce drag and upstream blowing caused vortex diffusion, the net energy was positive for all tested circular jet cases. The main reason for this is the significantly high jet velocity ratio, which can also be deduced from Equation (3).

3.2 High aspect ratio jets

Continuous blowing via high aspect ratio slot jets was subsequently tested, in order to address the energy inefficiencies measured for circular jets. These reduced the jet velocity ratio due to the increase in cross-sectional area, hence lowering the energy input, according to Equation 3. The total jet momentum coefficient was again set constant at C_μ = 0.02.

Four surface-normal jets of differing length and location were positioned along the line defined by the coordinates (x'_j/c = 0.1, z_j/D = ±0.236) and (x'_j/c = 0.3, z_j/D = ±0.405). The drag reduction varied slightly between $\Delta C_D/C_{D0}$ = -0.6% and $\Delta C_D/C_{D0}$ = -1.8%, while the net energy increase was around P_{net}/P_{D0} = 3% for all four cases. This is

summarizd for all four cases in Table 1. The reduction in drag coefficient is noticeably less than the $\Delta C_D/C_{D0}$ = -2.7% achieved with the pair of circular surface-normal jets (Fig. 5c). The expected drag reduction from the theoretical jet thrust is $\Delta C_D/C_{D0}$ = -2.4%, suggesting that there is an adverse effect caused by the slot jets. This configuration was not investigated any further.

Table 1. Cases of surface-normal slot jet.

No.	Start (x'_j/c)	End (x'_j/c)	Length (mm)	$\Delta C_D/C_{D0}$	P_{net}/P_{D0}
1	0.10	0.25	30	-0.6%	3.6%
2	0.10	0.20	20	-1.5%	3.1%
3	0.15	0.25	20	-1.7%	2.9%
4	0.20	0.30	20	-1.8%	2.8%

For the spanwise slot blowing case defined in Fig. 4c, the drag coefficient increased by $\Delta C_D/C_{D0}$ = 5.0%, with a corresponding net energy increase of P_{net}/P_{D0} = 9%. The drag coefficient of seven additional slots were tested, of lengths ranging from 19 mm to 47.5 mm, and which were positioned between x'_j/c = 0.05 and x'_j/c = 0.3, along an extension of the line defining the slot in Fig. 4c. For these cases, the increase in drag coefficient ranged between $\Delta C_D/C_{D0}$ = 4.0% and $\Delta C_D/C_{D0}$ = 6.8%, with the net energy between P_{net}/P_{D0} = 9% and P_{net}/P_{D0} = 11%. This is summarized for all eight cases in Table 2.

Table 2. Cases of spanwise slot jet.

No.	Start (x'_j/c)	End (x'_j/c)	Length ($\Delta x'_j/c$)	$\Delta C_D/C_{D0}$	P_{net}/P_{D0}
1	0.05	0.30	0.25	6.3%	8.7%
2	0.05	0.20	0.15	6.3%	10.2%
3	0.10	0.25	0.15	5.0%	9.2%
4	0.15	0.30	0.15	6.8%	10.7%
5	0.05	0.15	0.1	4.3%	9.0%
6	0.10	0.20	0.1	4.0%	8.7%
7	0.15	0.25	0.1	4.8%	9.5%
8	0.20	0.30	0.1	5.0%	9.7%

The time-averaged crossflow vorticity for the case described in Fig. 4c (case No. 3 in

Table 2) is presented in Fig. 10. The spanwise blowing from the jets causes two regions of concentrated vorticity in the shear layer, with the outer edge of the shear layer forming further outboard, beyond the edge of the upsweep (Fig. 10a). The subsequent afterbody vortices at x/L = 0.4 (Fig. 10b) appear more diffuse and disorganized. The vortex cores at x/L = 0.4 and x/L = 0.6 (Fig. 10c) are deflected away from the upswept face, as also observed with wing tip vortices following spanwise blowing from the tips [18, 20]. The vortices at the final two stations appear more diffuse than the baseline (Fig. 10d and Fig. 10e). The larger drag coefficient is likely to be a result of an increase in the width of the wake, caused by the jets deflecting streamlines away from the afterbody. The strengthening of the shear layer at the upstream stations is expected to contribute towards an increase in the magnitude of low pressure on the upswept surface.

The effect of the jet flap incidence angle on the drag reduction and net energy savings is shown in Fig. 11, and compared against the contribution from the theoretical jet thrust component. Generally, with increasing jet angle, the magnitude of drag reduction lessens. The greatest improvement in the drag coefficient occurs for α_j = 30°, when the jet is almost parallel to the freestream (Fig. 11a). At this angle, the drag reduction totals $\Delta C_D/C_{D0}$ = -8.6%, with a corresponding net energy reduction of around P_{net}/P_{D0} = -3% (Fig. 11b). At angles greater than α_j = 45°, the measured drag reductions are less than the thrust contributions. For larger angles, there is a risk that the jet is deflecting the streamlines as the flow passes the upstream apex of the upsweep, thereby increasing the height, and area, of the wake.

The time-averaged vorticity field for the α_j = 30° jet flap case is shown in Fig. 12. At x/L = 0.2 (Fig. 12a), small jet vortices generated at the tips of the jet flap restrict the

formation of the developing shear layer such that it is shorter, but more intense than the baseline. The size of the vortex cores at $x/L = 0.4$ (Fig. 12b) and $x/L = 0.6$ (Fig. 12c) are reduced, with the vortices displaced slightly away from the surface. There is little difference in the peak vorticity between the baseline and flow control cases at $x/L = 0.8$ (Fig. 12d) and at the trailing edge (Fig. 12e), but the size of the vortex cores appears slightly reduced. Figure 13 shows that the circulation of the time-averaged vortex is noticeably reduced across all streamwise stations for $x/L \geq 0.4$, with reductions of over 16% at $x/L = 0.4$. This lower vortex circulation, coupled with a displacement away from the upswept surface, is likely to result in an increased surface pressure, leading to the significant drag reductions that were measured.

3.3 Pulsed Blowing

As the jet flap blowing at $\alpha_j = 30°$ showed the most promising energy saving results, this jet configuration was used for the subsequent pulsed blowing study. The motivations for exploring the effects of pulsed blowing were twofold. The first was to reduce the mass flux, hence power supplied to the jet, and the second was to exploit any additional favourable jet/vortex interactions. The peak C_μ was fixed at $C_\mu = 0.02$ for all pulsed blowing cases, while the pulsing frequency, f, and duty cycle of the input square pulse were varied. Obviously, the mean momentum coefficient increases with the increasing duty cycle.

The effect of reduced frequency fD/U_∞ on the drag reduction and net energy savings is shown in Figure 14 for various values of the duty cycle. The drag reduction exhibits an increasing trend with the reduced frequency, whereas the variation of the net energy savings is smaller. There is a suggestion of small peaks around $fD/U_\infty \approx 0.4$ and 0.6,

but the data are inconclusive. It is interesting that, for an Ahmed body [22], it was found that the optimal reduced frequency is around 0.5. We cannot confirm this for our geometry. There is a need for further research in a frequency range wider than tested in the current experiments in order to fully explore the effect of frequency.

A much better collapse of the data are found if the drag reduction and net energy savings are plotted as a function of mean momentum coefficient in Figure 15. For almost all pulsed jet cases, the drag reduction is larger than for the equivalent continuous blowing case at the same $\overline{C}_\mu$ (Fig. 15a). The same is true for energy savings (Fig. 15b). For both plots in Figure 15, the data for the pulsing jets seem to approach the continuous blowing case with increasing momentum coefficient. A maximum of around 9% reduction in the drag and 6% of the net energy savings are observed.

The time-averaged crossflow vorticity of the best performing pulsed blowing case ($\overline{C}_\mu = 0.0125$, $fD/U_\infty = 0.62$) is shown alongside the baseline in Fig. 16. At $x/L = 0.2$ (Fig. 16a), the extent of the shear layer has been displaced outboard, similar to that caused by continuous blowing (Fig. 12a). At the subsequent measurement plane, $x/L = 0.4$, the vortex cores are smaller and further outboard (Fig. 16b), while downstream at $x/L = 0.6$ they have been displaced away from the upswept surface (Fig. 16c). The vortices at the final two measurement planes appear slightly weaker than the baseline (Fig. 16d and Fig. 16e), while the vortex cores appear slightly smaller.

The time-averaged vortex circulation of the pulsed blowing case is compared against the baseline and the equivalent continuous blowing case at the same time-averaged jet momentum coefficient ($\overline{C}_\mu = 0.0125$, $f = 0$) in Fig. 17. Both flow control cases result in vortices with a larger circulation than the baseline, for stations upstream of $x/L = 0.2$,

but with a smaller circulation downstream. The vortex circulation is lower for the pulsed blowing case than continuous blowing at all measured streamwise locations, although the difference is small (less than 10%).

The locations of the time-averaged vortex centroids are found from the first-order moment of vorticity in the z and y directions [25]. Figure 18a compares the relative strength of the time-averaged vortices by including the distance from the wall of the vortex centroids, $\Gamma/U_\infty \overline{h}$. The circulation non-dimensionalized by the distance from the wall is a measure of the velocity induced by the vortex, hence is related to pressure and drag force. This figure shows that the relative circulation of the vortices of the baseline case gradually decay, following the initial increase at the upstream locations. Generally, both continuous blowing and pulsed blowing have lower relative strength. At the upstream locations the vortices are weaker for pulsed blowing, however after $x/L \geq 0.6$ the two merge. The largest change in spanwise separation occurs at the furthest upstream station, $x/L = 0.2$, where the vortices are spaced further apart than the baseline by around 10% of the fuselage diameter for both blowing cases (Fig. 18b). This tends to baseline levels towards the trailing edge. The spanwise separation of vortices subjected to pulsed blowing is noticeably greater than continuous blowing at all streamwise stations, with a maximum separation increase of 12% of the diameter at $x/L = 0.2$. This increase in spanwise separation is expected to result in a lower induced velocity towards the surface, near the centreline. In addition, the vortex footprint area becomes smaller with increasing spanwise separation as the vortices are located further outboard.

Phase-averaged vorticity of the pulsed blowing case is presented in Fig. 19 for four different phases along the jet pulse cycle. The five measurement planes in each 3D plot correspond to x/L = 0.2, 0.4, 0.6, 0.8, and 1.0. At the furthest upstream station, x/L = 0.2, the shear layer appears similar to the time-averaged case when t/T = 0 and t/T = 0.25 before being pushed away from the surface when t/T = 0.5. At x/L = 0.4, the phase-to-phase variation is not as apparent, but the vortices appear broken and slightly diffuse when t/T = 0.75. At x/L = 0.6, the vortices are at their weakest and most diffuse when t/T = 0. At the next phase measurement, t/T = 0.25, although the vortices have increased in strength slightly, they are deflected further away from the surface, before they increase in strength at subsequent phases. The phase-to-phase variation becomes less noticeable at further downstream locations. At x/L = 0.8, when t/T = 0, the vortices appear slightly stronger than subsequent phases - they weaken when t/T = 0.25 and t/T = 0.5. At the trailing edge, x/L = 1.0, the first three phase-locked results (t/T = 0 to t/T = 0.5) are almost identical, whereas the vortices appear slightly weakened when t/T = 0.75.

The vorticity and accompanying streamlines at z = 0 is shown in Fig. 20 for the baseline and both blowing cases. There is a thicker time-averaged boundary layer along the upswept centreline for the baseline and continuous blowing cases (Fig. 20a and Fig. 20b), indicated by a stronger and larger band of vorticity. This may suggest a weakly separated flow at the beginning of the swept surface and possibly a very thin recirculation bubble, however this cannot be confirmed with the current measurements near the wall. We note that similar measurements for a Reynolds number ten times larger did not reveal any observable bubble in the wind tunnel experiments [26]. In the current experiments we believe that the drag is mainly affected by the afterbody

vortices, and the recirculation bubble, if any, does not play a major role. The boundary layer is apparently less thick for the pulsed blowing case (Fig. 20c), most likely due to the turbulent mixing caused by the periodic jet. The phase-locked measurements reveal the effect of the jet as it travels downstream, although the jet flap is angled at $\alpha_j = 30°$. The effect of the jet is seen within the boundary layer, as indicated in Fig. 20d by a band of negative vorticity. As this decelerates downstream, it causes the boundary layer to thicken at $x/L = 0.4$. The following phase, $t/T = 0.25$, (Fig. 20e) shows that the thickened region has travelled downstream to approximately $x/L = 0.5$, accompanied by a small downward deflection of the streamlines. This is the same phase in the cycle where the vortices are displaced away from the surface at the nearby crossflow station, $x/L = 0.6$ (Fig. 19b). This suggests that the local thickening of the boundary layer from the jet pulse influences the displacement of the vortices. The jet then recommences its pulse cycle when $t/T = 0.5$ (Fig. 20f). The effects of the previous jet pulse can be seen at around $x/L = 0.7$ in this phase. Again, a downward displacement in the vortices is shown at $x/L = 0.2$ and $x/L = 0.8$ (Fig. 19c) coinciding with the streamline deflection shown in the symmetry plane. As the front of the jet reaches $x/L = 0.3$ by $t/T = 0.75$ (Fig. 20g), the effects of this are shown by the diffuse vortex at $x/L = 0.4$ in Fig. 19d. The phase-locked measurements show that streamline deflections away from the surface generally occur downstream of $x/L = 0.4$, but streamline deflections towards the surface are shown upstream of $x/L = 0.4$ when $t/T = 0$ and $t/T = 0.75$ for pulsed blowing (Fig. 20d and Fig. 20g), and for continuous blowing (Fig. 20b).

The crossflow RMS velocity at three upstream stations is shown in Fig. 21 for both blowing cases. The unsteadiness within the vortex cores for the pulsed blowing case is significantly larger than the continuous blowing example and is a result of the phase-

to-phase meandering of the vortices shown in Fig. 19. This increase in vortex meandering and turbulence ingestion [14], combined with an increase in spanwise vortex separation and reduction in circulation is likely to lead to the drag reduction and energy saving improvements for pulsed blowing.

4 Conclusions

Drag reduction, net power savings, and the efficacy of active flow control on modifying the formation of the counter-rotating vortex pair over an afterbody of a slanted base cyclinder were investigated in a water tunnel. Continuous blowing from circular jets and high aspect ratio slots, as well as pulsed blowing, were studied. The experiments included force and velocity measurements for various blowing configurations.

Drag reductions from continuous blowing through circular jets on the upswept face were highly dependent on blowing direction and location. These savings reached 7% when blowing outboard at further upstream and inboard locations, caused by jet vortices restricting the shear layer development, which lead to the formation of smaller vortex cores further away from the surface. Upstream blowing into the vortex core resulted in rapid diffusion of the vortices, but at the expense of an increase in drag. For all circular jet cases tested, there was a net energy increase, mainly due to the high jet velocity.

These energy inefficiencies were addressed through high aspect ratio jets to reduce the jet velocity and input energy. Spanwise blowing through slots on the upsweep edge deflected the vortices away from the surface, but resulted in a drag increase. A jet flap angled at $\alpha_j = 30°$ achieved drag reductions close to 9%, equating to energy savings of

almost 3%. Jet vortices shortened the shear layer, resulting in weaker afterbody vortices, further from the surface, and with lower circulation.

Pulsing the jet flap resulted in higher drag reductions and energy savings compared to the continuous blowing case with the same time-averaged momentum coefficient. There is no evidence of optimal frequencies. There was better collapse of the data when plotted as a function of time-averaged momentum coefficient. Pulsed blowing resulted in reductions of crossflow vortex circulation worth around 10% of the continuous blowing case at further upstream stations. Phase-locked PIV results indicated cyclic variations of the distance between the vortices and the surface, which coincided with the local thickening of the boundary layer caused by the periodic nature of the jet. The spanwise separation of the time-averaged centroids increased noticeably with pulsed blowing, while the crossflow turbulence intensity was larger than for continuous blowing due to significant phase-to-phase meandering.

Acknowledgements

This work was supported by the Air Force Office of Scientific Research, Air Force Material Command, USAF, under grant number FA9550-14-1-0126, monitored by Dr. Douglas Smith.

References

1. Bearman, P. W., "Bluff Body Flows Applicable to Vehicle Aerodynamics," *Journal of Fluids Engineering,* Vol. 102, No. 3, 1980, pp. 265-274. https://doi.org/10.1115/1.3240679

2. Bulathsinghala, D., Wang, Z., and Gursul, I., "Effect of Upsweep Angle on Afterbody Vortices," AIAA-2016-4344, *AIAA 46th Fluid Dynamics Conference*, AIAA, Reston, VA, 2016. https://doi.org/10.2514/6.2016-4344

3. Thomas, A. S., Saric, W. S., Braslow, A. L., Bushnell, D. M., Lock, R. C. and Hackett, J. E., "Aircraft Drag Prediction and Reduction," *AGARD Report No. 723*, 1985, pp. 1-6.

4. Epstein, R. J., Carbonaro, M. C., and Caudron, F., "Experimental Investigation of the Flowfield About an Upswept Afterbody," *Journal of Aircraft,* Vol. 31, No. 6, 1994, pp. 1281-1290. https://doi.org/10.2514/6.1994-1840

5. Bury, Y., Jardin, T. and Klockner, A., "Experimental Investigation of the Vortical Activity in the Close Wake of a Simplified Military Transport Aircraft," *Experiments in Fluids*, Vol. 54, No. 5, 2013, pp. 1-15. https://doi.org/10.1007/s00348-013-1524-4

6. Jackson, R., Wang, Z., and Gursul, I., "Control of Afterbody Vortices by Blowing," AIAA-2015-2777, *AIAA 45th Fluid Dynamics Conference*, AIAA, Reston, VA, 2015. https://doi.org/10.2514/6.2015-2777

7. Bulathsinghala, D., Jackson, R., Wang, Z., and Gursul, I., "Afterbody Vortices of Axisymmetric Cylinders with a Slanted Base," *Experiments in Fluids*, Vol. 58, No. 5, 2017, pp. 1-24. https://doi.org/10.1007/s00348-017-2343-9

8. Britcher, C. P., and Alcorn, C. W., "Interference-Free Measurements of the Subsonic Aerodynamics of Slanted-Base Ogive Cylinders," *AIAA Journal,* Vol. 29, No. 4, 1991, pp. 520-525. https://doi.org/10.2514/3.10614

9. McCluney, B. and Marshall, J., "Drag Development of the Belfast," *Aircraft Engineering and Aerospace Technology,* Vol. 39, No. 10, 1967, pp. 33-37. https://doi.org/10.1108/eb034302

10. Calarese, W., Crisler, W. P., and Gustafson, G. L., "Afterbody Drag Reduction by Vortex Generators," AIAA-1985-0354, *AIAA 23rd Aerospace Sciences Meeting,* AIAA, New York, NY, 1985. https://doi.org/10.2514/6.1985-354

11. Wortman, A., "Reduction of Fuselage Form Drag by Vortex Flows," *Journal of Aircraft,* Vol. 36, No. 3, 1999, pp. 501-506. https://doi.org/10.2514/2.2484

12. Smith, B. R., Yagle, P. J. and Hooker, J. R., "Reduction of Aft Fuselage Drag on the C-130 Using Microvanes," AIAA- 2013-0105, *AIAA 51st Aerospace Sciences Meeting,* AIAA, Reston, VA, 2013. https://doi.org/10.2514/6.2013-105

13. Bulathsinghala, D., Wang, Z. and Gursul, I., "Drag Reduction by Manipulation of Afterbody Vortices, *Journal of Aircraft*, Volume 55, Number 6, November 2018. https://doi.org/10.2514/1.C034957

14. Gursul, I. and Wang, Z. "Flow Control of Tip/Edge Vortices", *AIAA Journal*, Special Issue on Flow Control, Volume 56, Number 5, May 2018. http://arc.aiaa.org/doi/abs/10.2514/1.J056586

15. Jackson, R., Wang, Z., and Gursul, I., "Afterbody Drag Reduction Using Active Flow Control," AIAA-2017-0954, *AIAA 55th Aerospace Sciences Meeting*, AIAA, Reston, VA, 2017. https://doi.org/10.2514/6.2017-0954

16. Phillips, W. R. C., and Graham, J. A. H., "Reynolds-Stress Measurements in a Turbulent Trailing Vortex," *Journal of Fluid Mechanics,* Vol. 147, Oct., 1984, pp. 353-371.
https://doi.org/10.1017/S0022112084002123

17. Margaris, P., Marles, D., and Gursul, I., "Experiments on Jet/Vortex Interaction," *Experiments in Fluids,* Vol. 44, No. 2, 2008, pp. 261-278.
https://doi.org/10.1007/s00348-007-0399-7

18. Margaris, P., and Gursul, I., "Vortex Topology of Wing Tip Blowing," *Aerospace Science and Technology,* Vol. 14, No. 3, 2010, pp. 143-160.
https://doi.org/10.1016/j.ast.2009.11.008

19. Hu, T., Wang, Z., and Gursul, I., "Passive Control of Roll Oscillations of Low-Aspect-Ratio Wings Using Bleed," *Experiments in Fluids,* Vol. 55, No. 6, 2014, pp. 1-16.
https://doi.org/10.1007/s00348-014-1752-2

20. Heyes, A., and Smith, D., "Spatial Perturbation of a Wing-tip Vortex Using Pulsed Span-wise Jets," *Experiments in Fluids,* Vol. 37, No. 1, 2004, pp. 120-127.
https://doi.org/10.1007/s00348-004-0791-5

21. Aubrun, S., McNally, J., Alvi, F., and Kourta, A., "Separation Flow Control on a Generic Ground Vehicle Using Steady Microjet Arrays," *Experiments in Fluids*, Vol. 51, No. 5, 2011, pp. 1177-1187.
https://doi.org/10.1007/s00348-011-1132-0

22. Joseph, P., Amandolese, X., and Aider, J., "Drag Reduction on the 25 Degree Slant Angle Ahmed Reference Body Using Pulsed Jets," *Experiments in Fluids*, Vol. 52, No. 5, 2012, pp. 1169-1185.
https://doi.org/10.1007/s00348-011-1245-5

23. Gillieron, P., and Kourta, A., "Aerodynamic Drag Control by Pulsed Jets on Simplified Car Geometry," *Experiments in Fluids*, Vol. 52, No. 2, 2013, pp. 1-16.
https://doi.org/10.1007/s00348-013-1457-y

24. Moffat, R.J., "Describing the Uncertainties in Experimental Results," *Experimental Thermal and Fluid Science*, Vol. 1, No. 1, 1988, pp. 3-17.
https://doi.org/10.1016/0894-1777(88)90043-X

25. Leweke, T., Le Dizès, S., and Williamson, C., "Dynamics and Instabilities of Vortex Pairs," *Annual Review of Fluid Mechanics*, Vol. 48, 2016, pp. 507-541.
https://doi.org/10.1146/annurev-fluid-122414-034558

26. Bulathsinghala, D.S., Wang, Z., and Gursul, I. "Modified near-wakes of axisymmetric cylinders with slanted base", *Aerospace Science and Technology*, vol. 86, 2019, pp. 351–363.
https://doi.org/10.1016/j.ast.2019.01.022

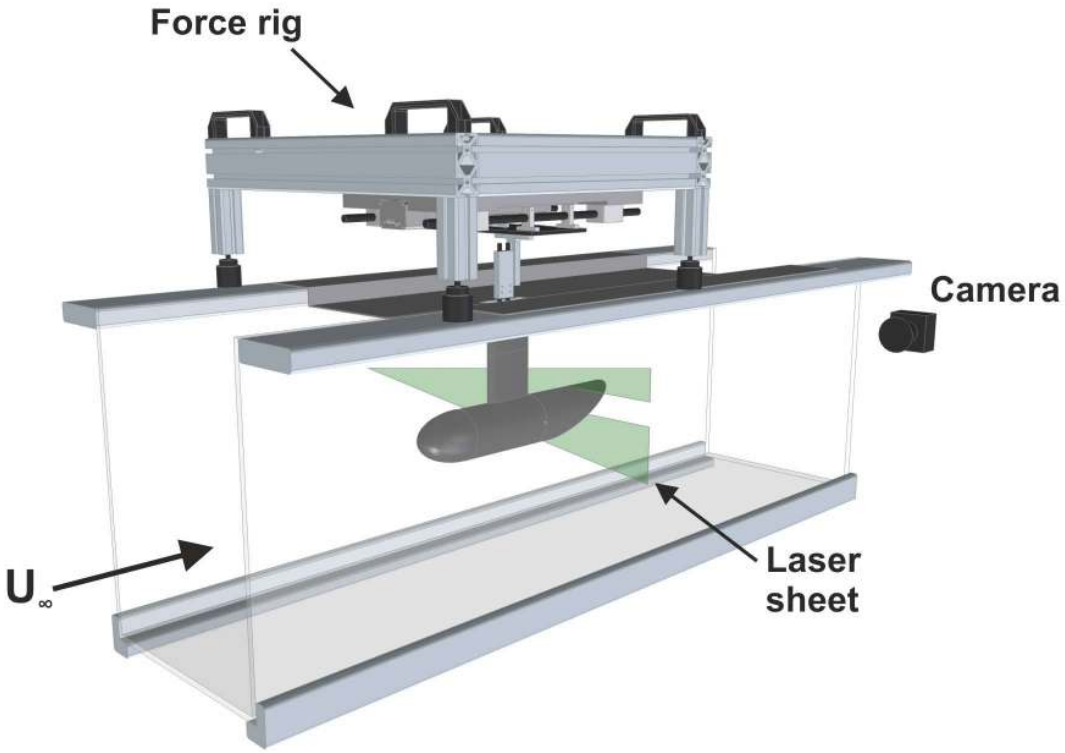

Figure 1. A schematic of the experimental setup in the water tunnel, showing the laser and camera positions for crossflow PIV measurements.

(a)

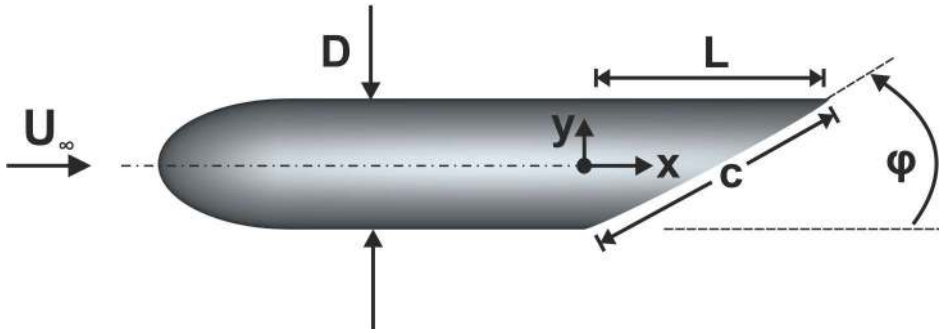

(b)

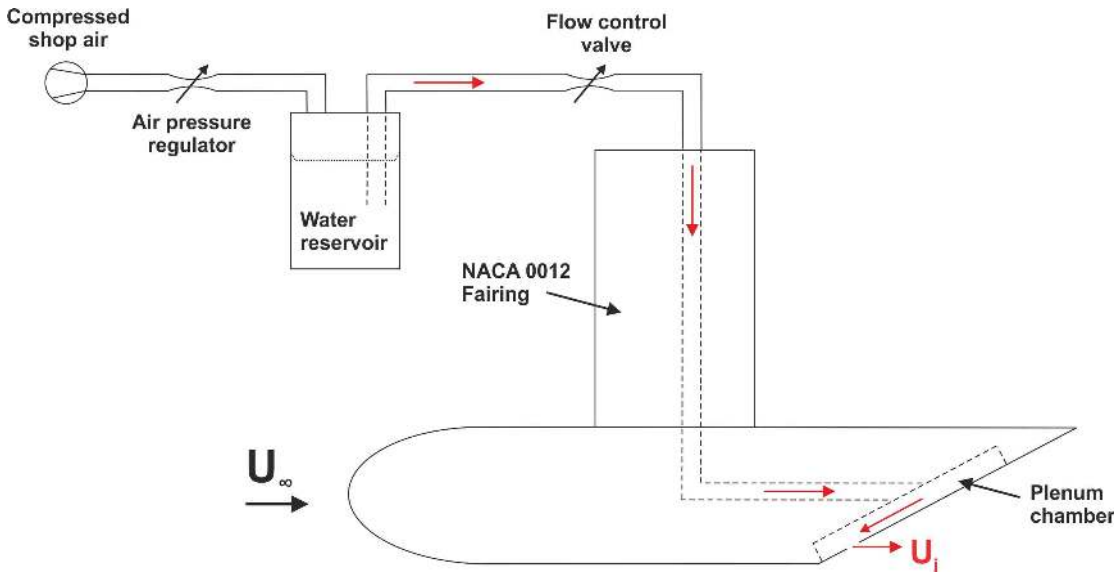

Figure 2. (a) Simplified fuselage model showing the axes and definitions of the basic dimensions; (b) schematic of the water supply.

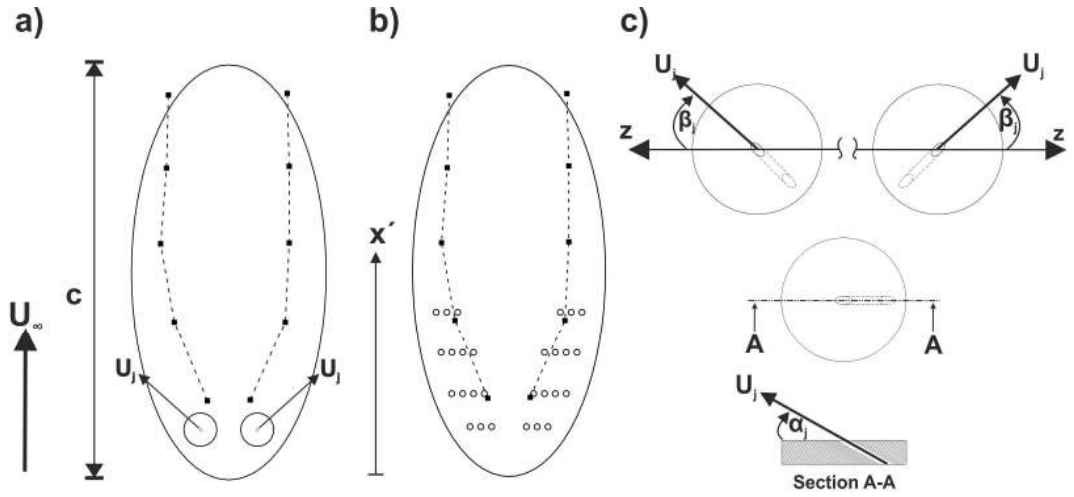

Figure 3. Key parameters for the circular jet configurations, showing a) the upswept face and the vortex trajectory for the baseline case, with one of the jet locations for reference, b) the positions of the different jet locations tested, and c) the definition of the yaw and incidence angles for the jets.

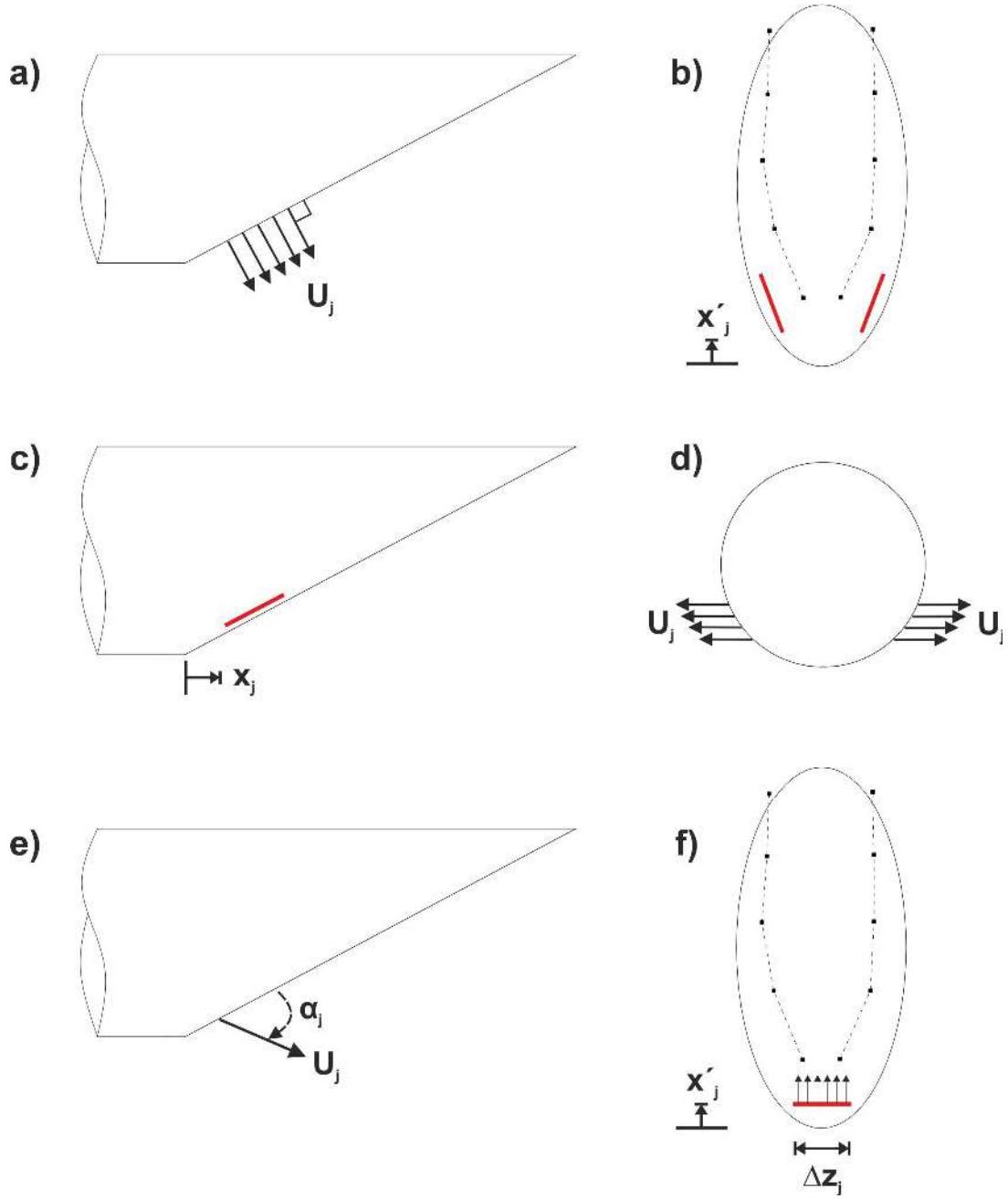

Figure 4. Definition of the high aspect ratio slot jets, showing a) and b), a pair of surface-normal jets, c) and d), a pair of spanwise jets, e) and f) a jet flap.

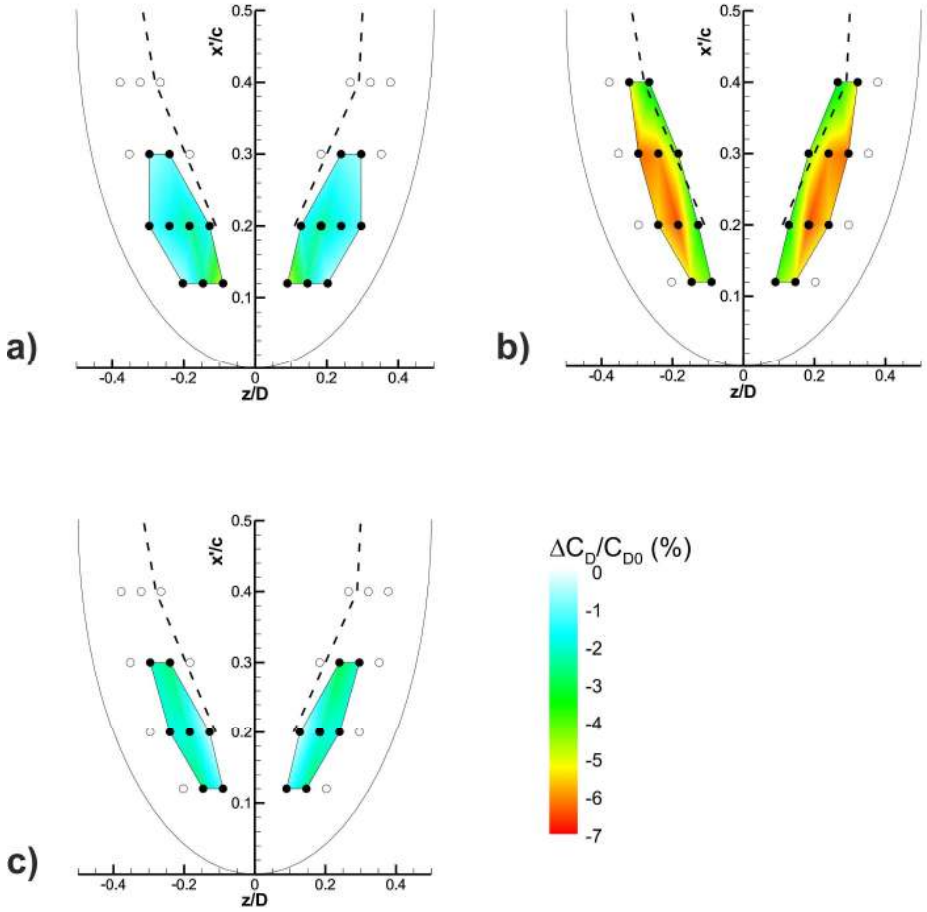

Figure 5. Drag reduction from circular jets as a function of jet location for three different jet directions: a) $\alpha_j = 30°$, $\beta_j = 0°$, b) $\alpha_j = 30°$, $\beta_j = 90°$ and c) $\alpha_j = 90°$. Filled holes indicate collected data.

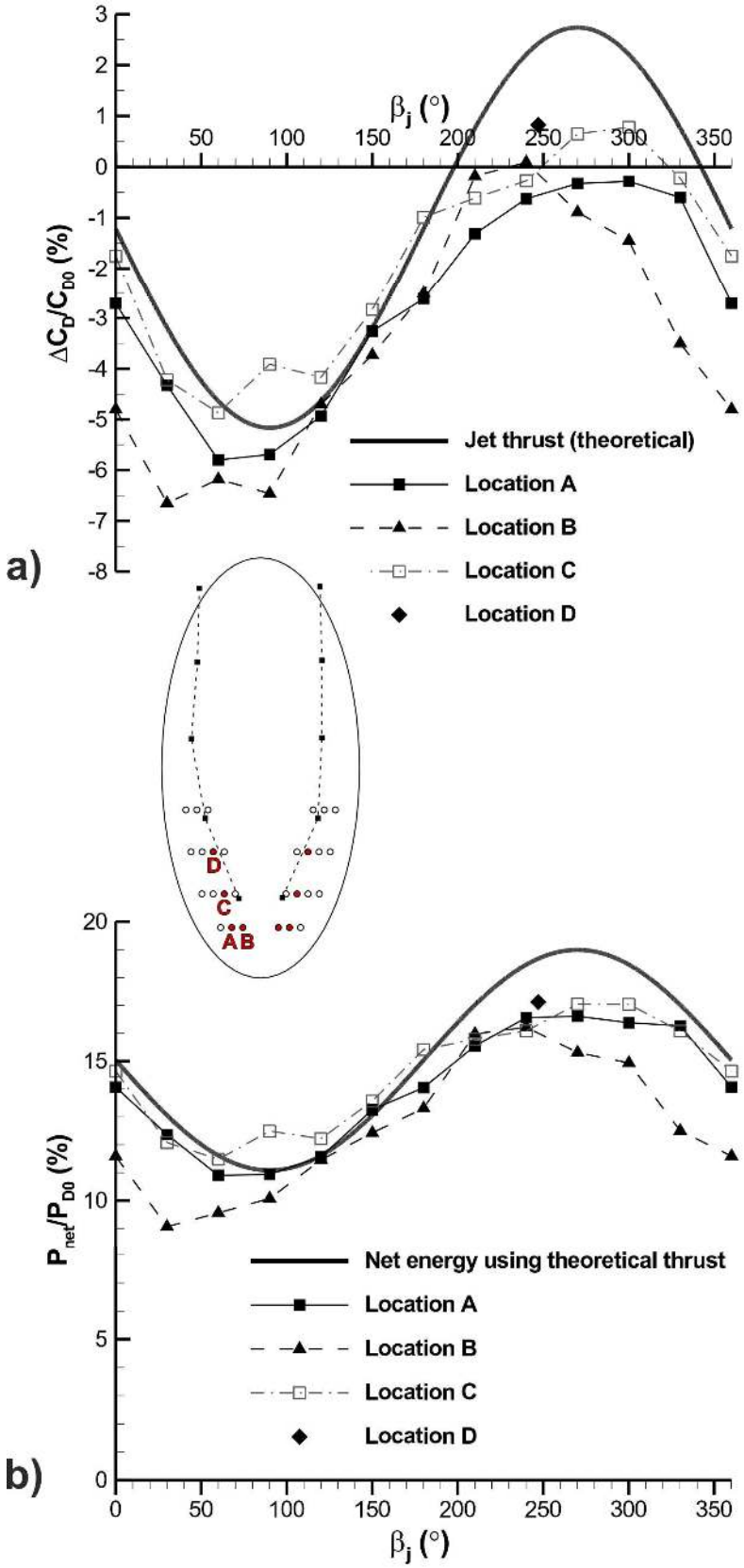

Figure 6. Effect of jet yaw angle, β_j, on a) the change in drag reduction and b) net energy for four jet locations.

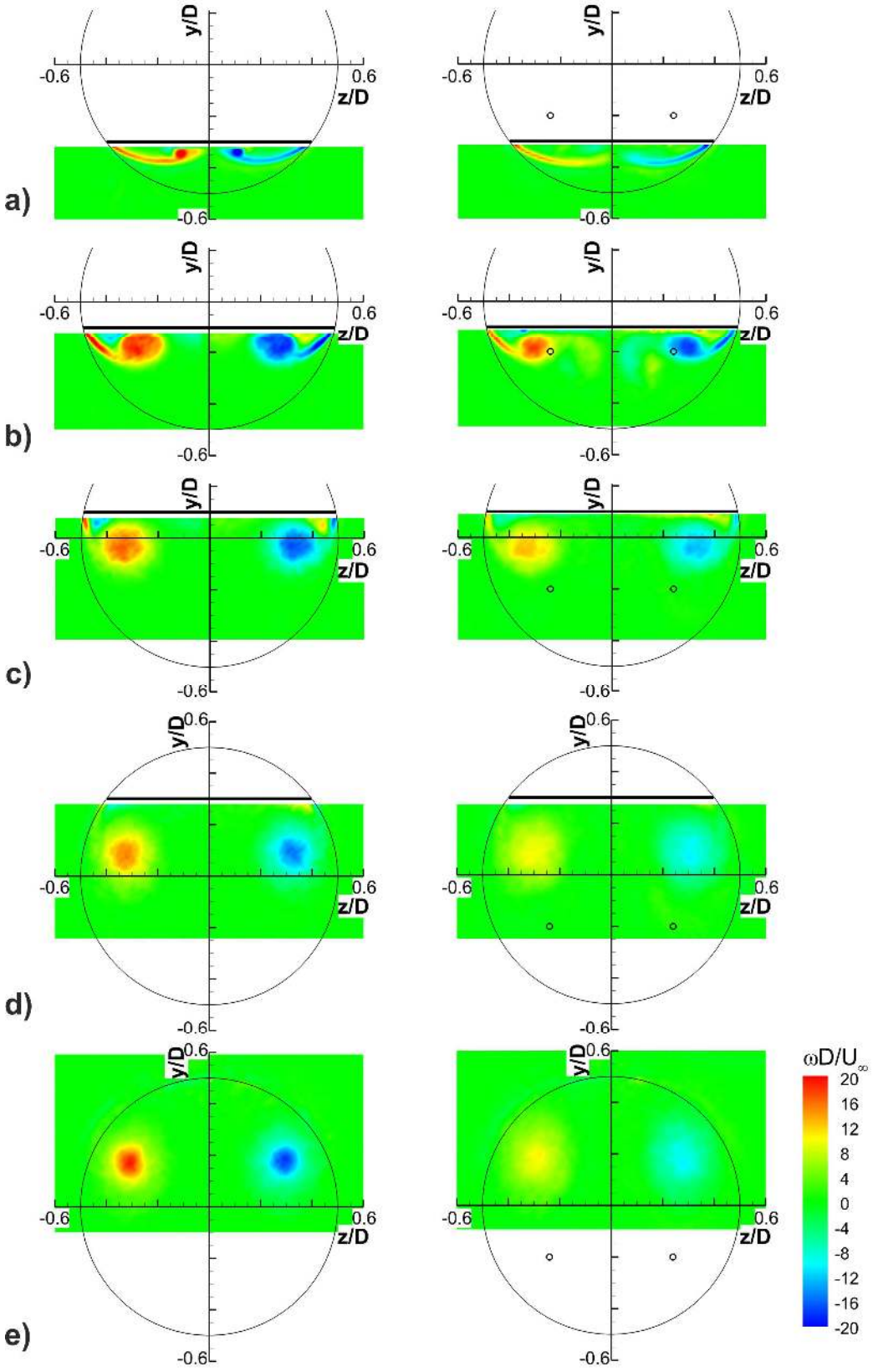

Figure 7. Time-averaged crossflow vorticity of the baseline case, left, and an upstream blowing case (Location D, $\alpha_j = 30°$, $\beta_j = 247°$), right. Jet positions are indicated by small, black circles. Measurement planes are located at a) x/L = 0.2, b) x/L = 0.4, c) x/L = 0.6, d) x/L = 0.8 and e) x/L = 1.0.

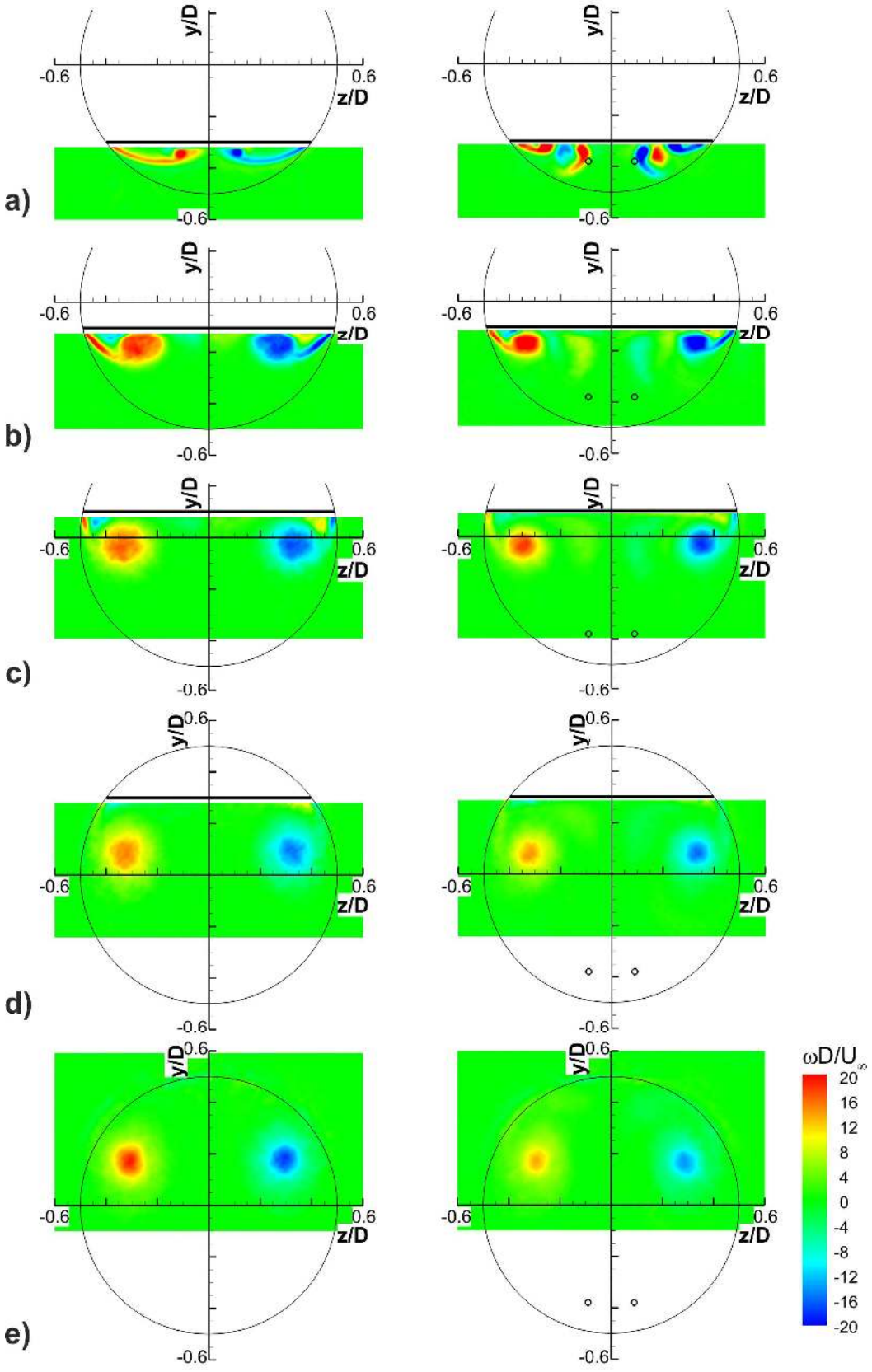

Figure 8. Time-averaged crossflow vorticity of the baseline case, left, and an outboard blowing case (Location B, α_j = 30°, β_j = 0°), right. Jet positions are indicated by small, black circles. Measurement planes are located at a) x/L = 0.2, b) x/L = 0.4, c) x/L = 0.6, d) x/L = 0.8 and e) x/L = 1.0.

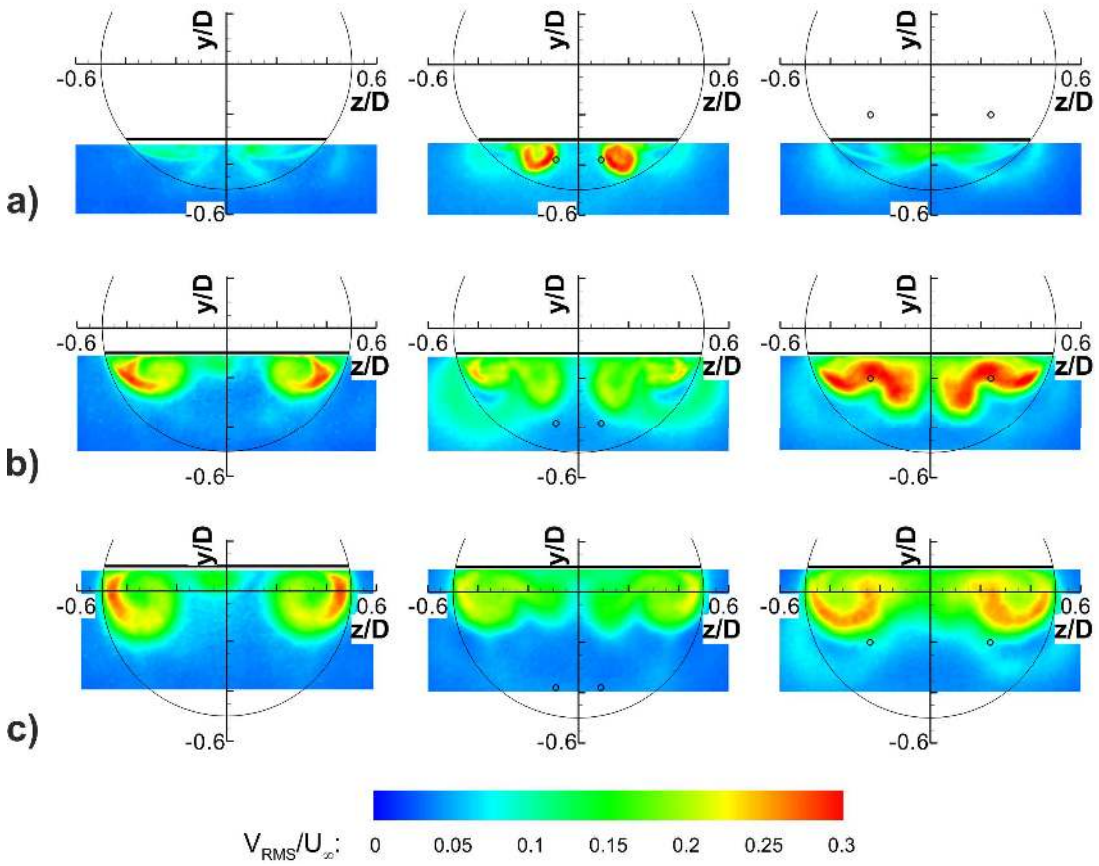

Figure 9. Crossflow RMS velocity of the baseline case, left, outboard blowing case, middle, and upstream blowing case, right. Jet positions are indicated by small, black circles. Measurement planes are located at a) x/L = 0.2, b) x/L = 0.4 and c) x/L = 0.6.

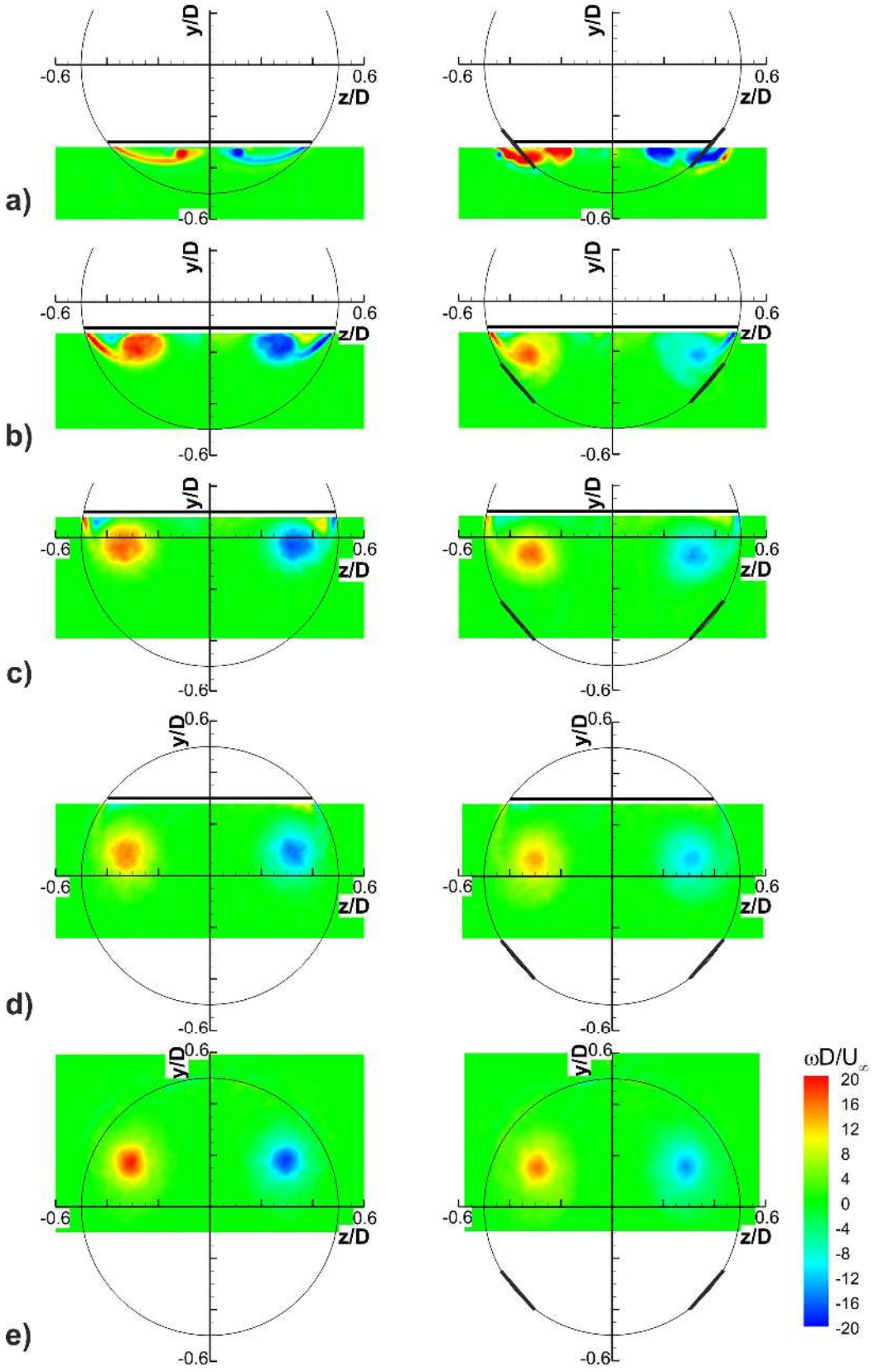

Figure 10. Time-averaged crossflow vorticity of the baseline case, left, and the spanwise slot jet case, right. Jet slots are indicated by thick, solid lines on the upsweep edge. Measurement planes are located at a) x/L = 0.2, b) x/L = 0.4, c) x/L = 0.6, d) x/L = 0.8 and e) x/L = 1.0.

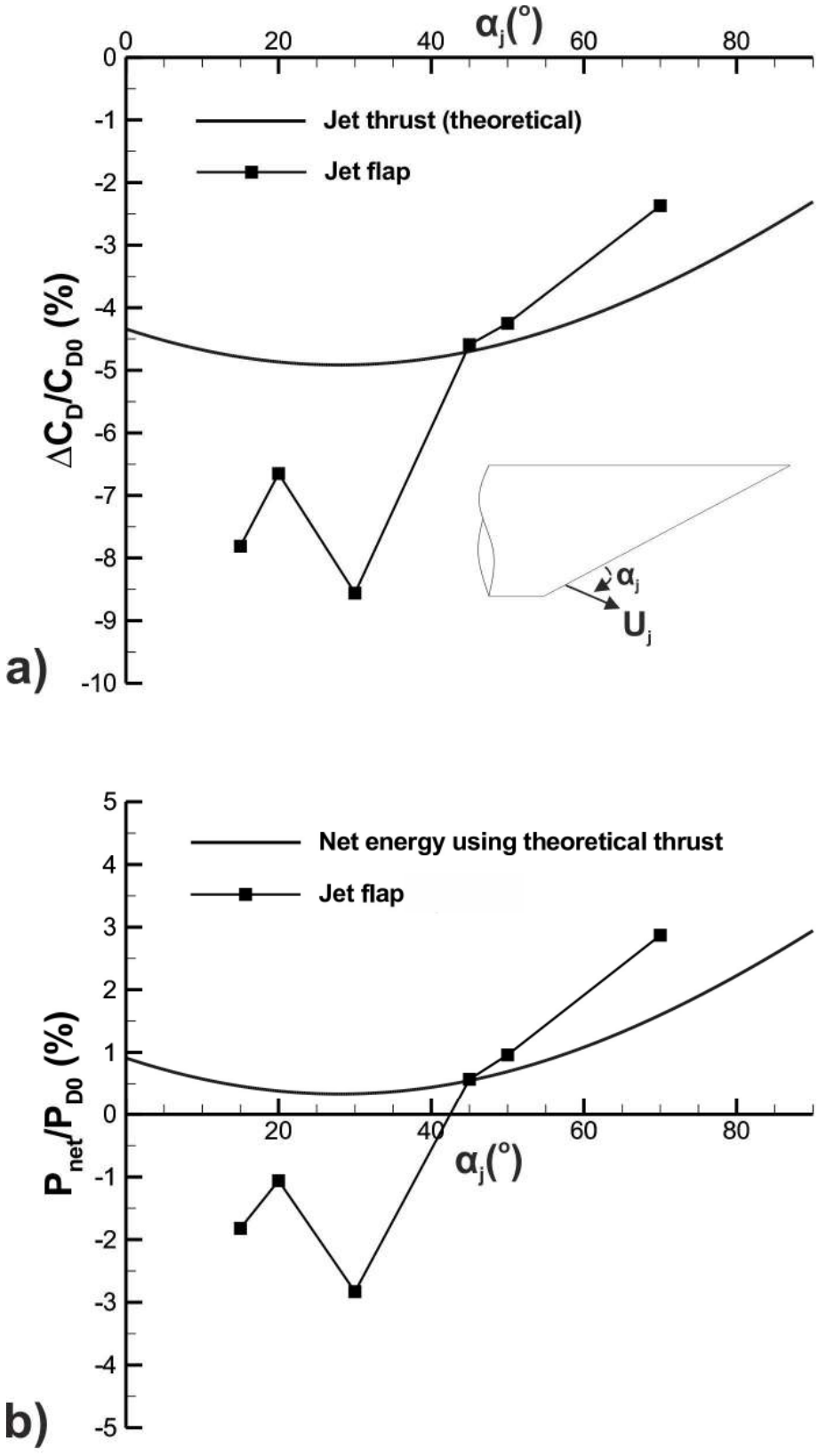

Figure 11. Change in drag reduction and net energy with α_j for the jet flap case.

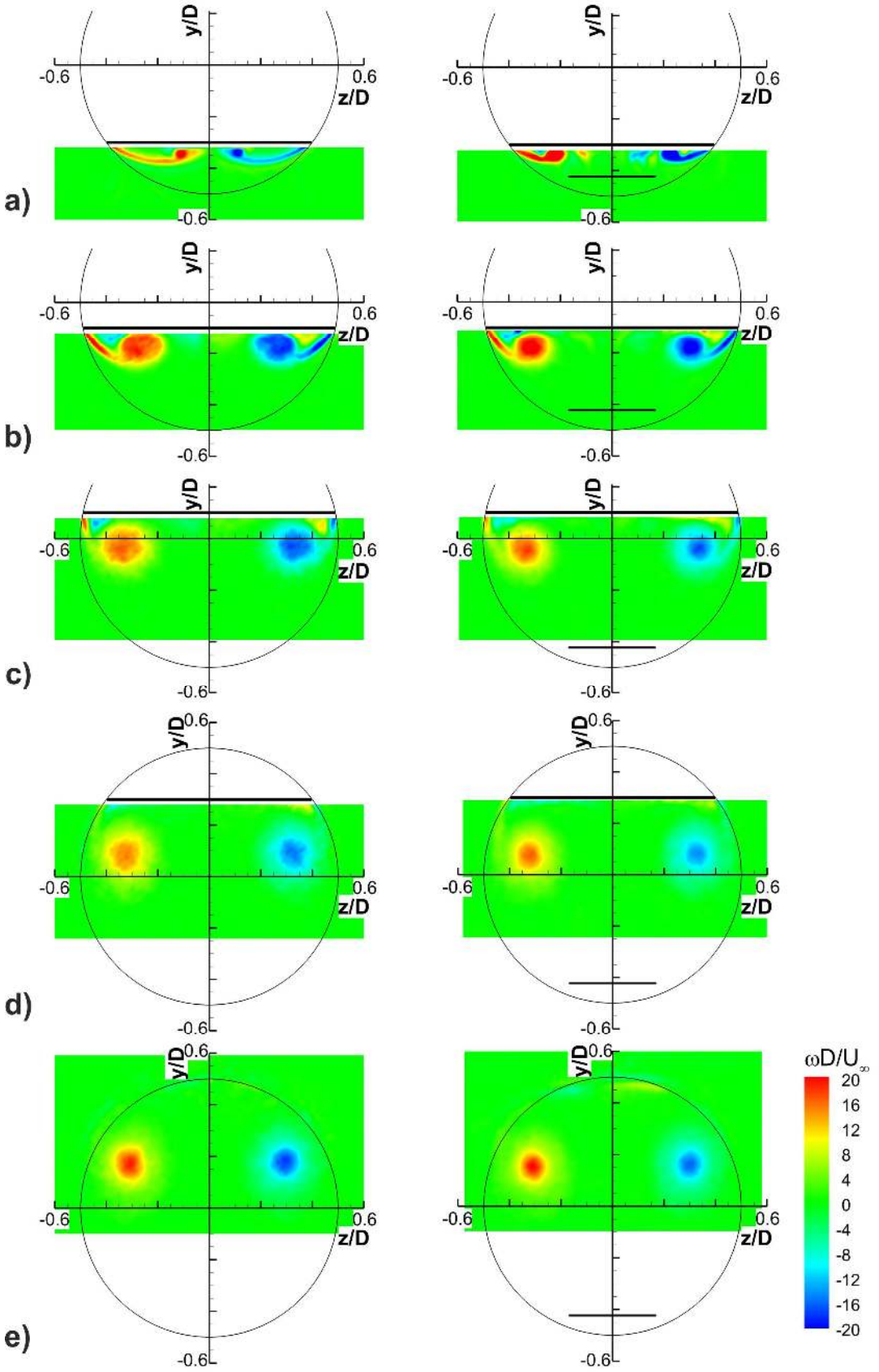

Figure 12. Time-averaged crossflow vorticity of the baseline case, left, and a jet flap case (α_j = 30°), right. Jet flap position is indicated on upswept face. Measurement planes are located at a) x/L = 0.2, b) x/L = 0.4, c) x/L = 0.6, d) x/L = 0.8 and e) x/L = 1.0.

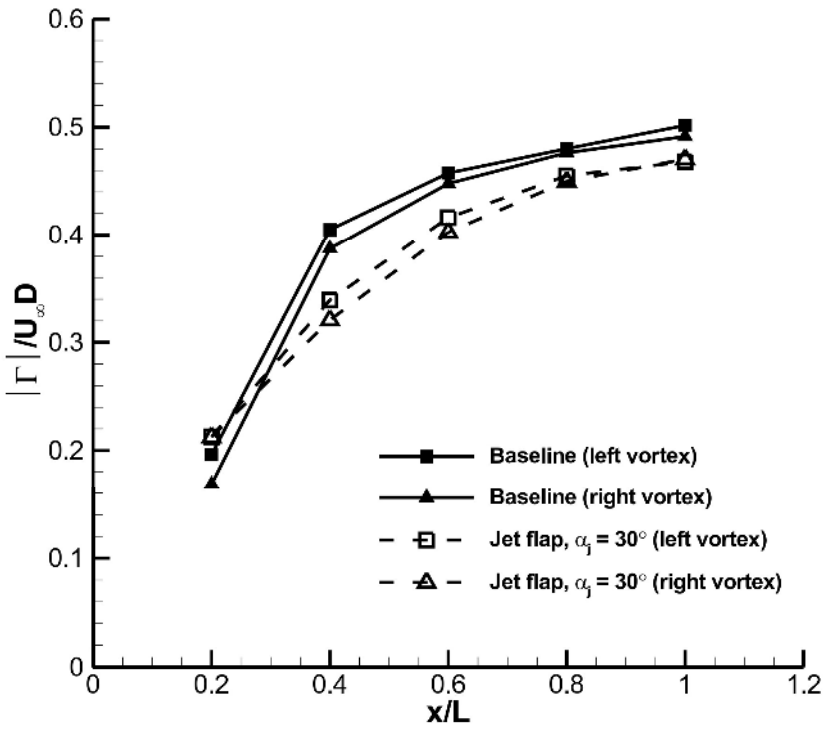

Figure 13. Development of crossflow vortex circulation with streamwise distance for the jet flap case ($\alpha_j = 30°$).

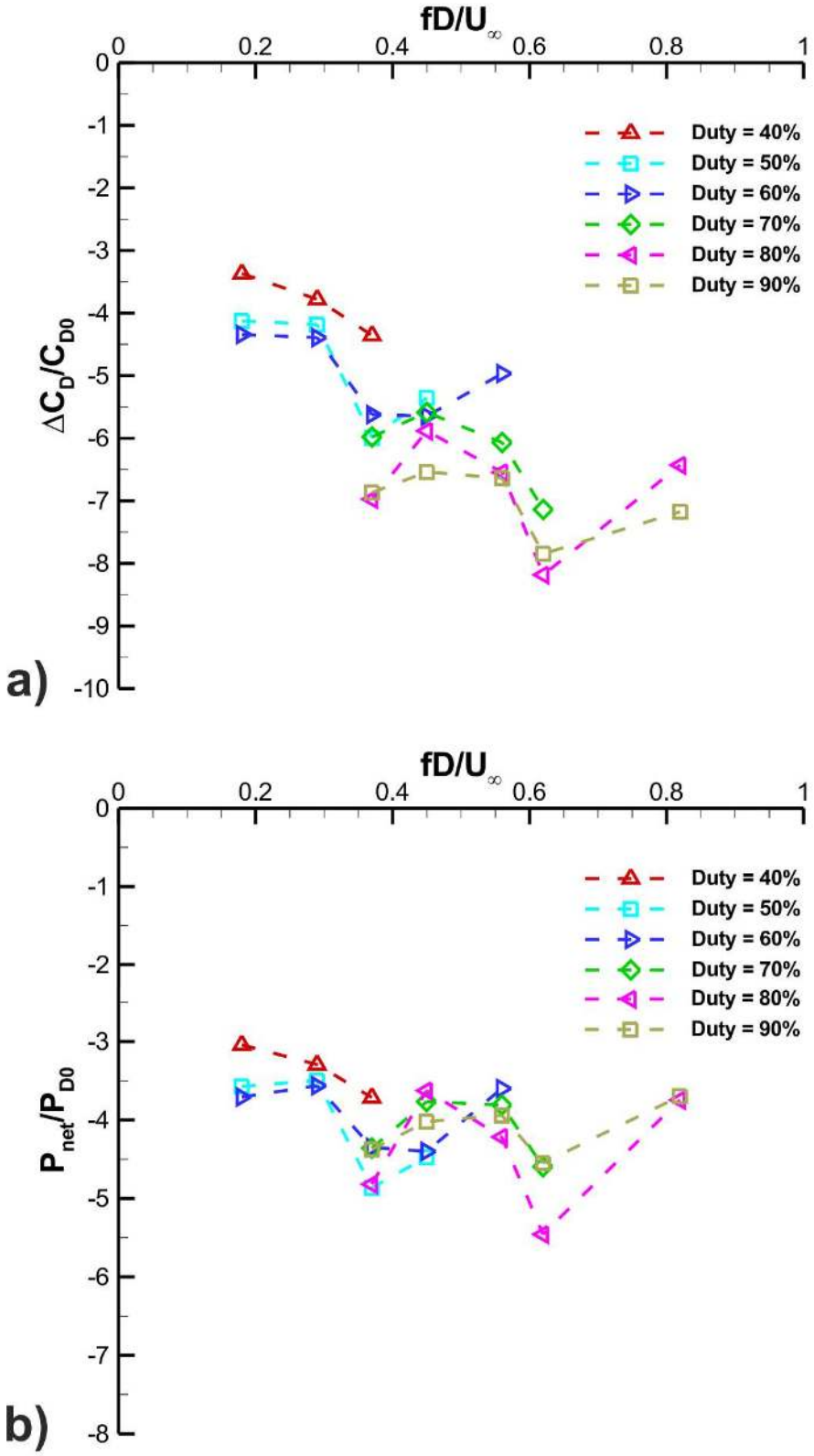

Figure 14. Change in drag coefficient (a) and net energy (b), as a function of reduced frequency and duty cycle, for the pulsed blowing cases.

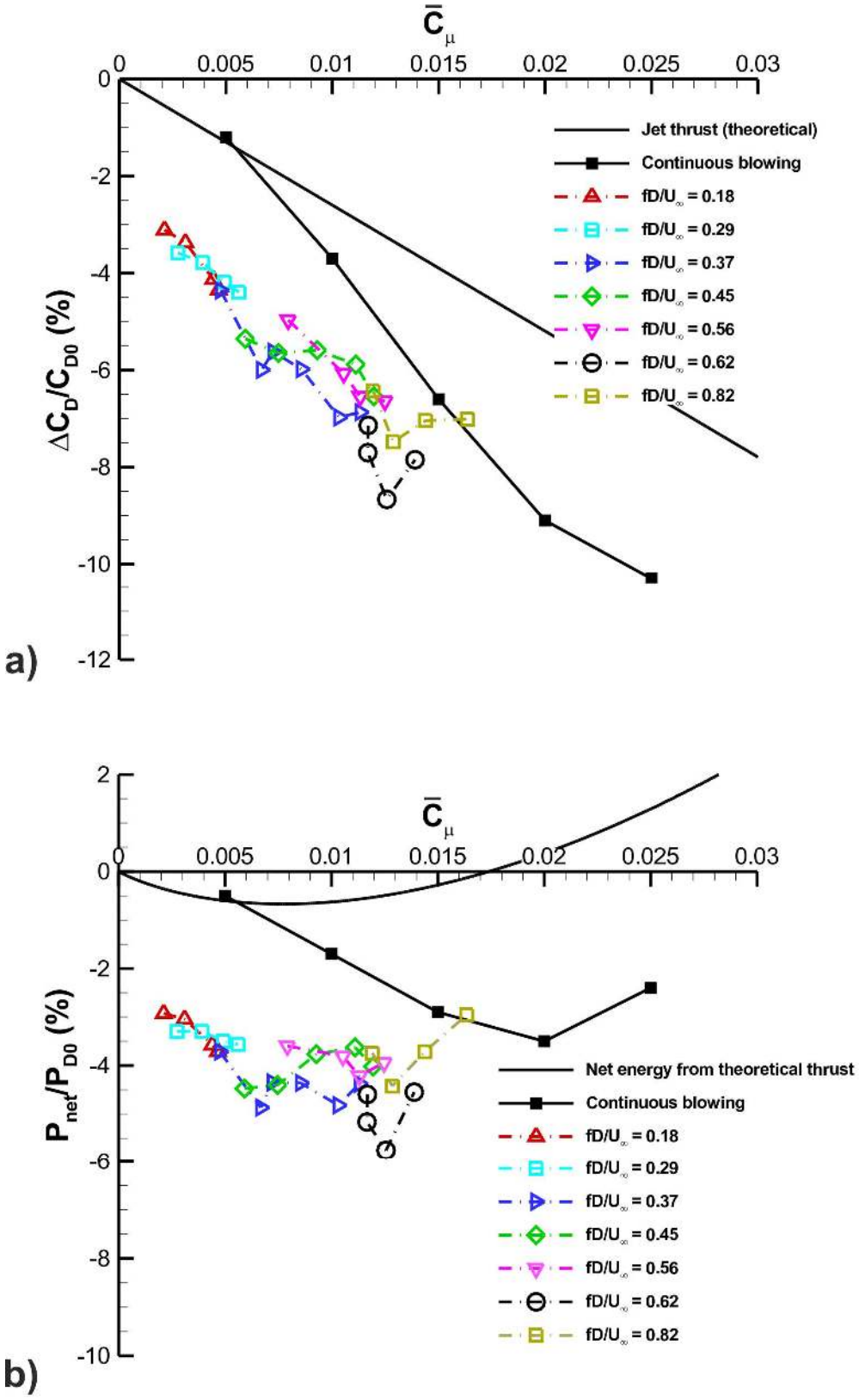

Figure 15. Effect of time-averaged jet momentum coefficient, $\bar{C}_\mu$, on a) the change in drag reduction and b) net energy, for a range of jet pulsing frequencies.

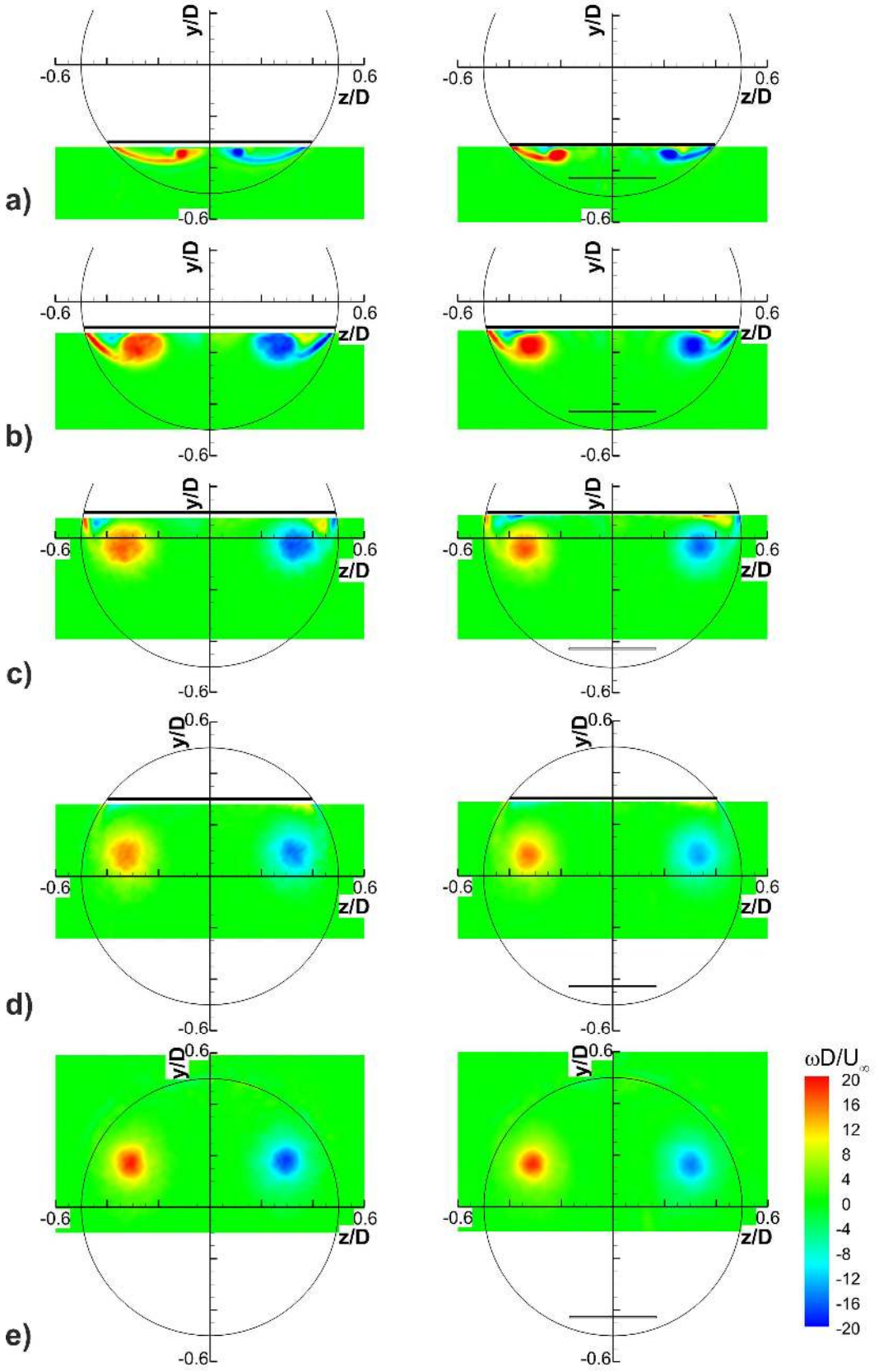

Figure 16. Time-averaged crossflow vorticity of the baseline case, left, and a pulsed blowing case ($\bar{C}_\mu$ = 0.0125, fD/U_∞ = 0.62), right. The jet flap is marked by a black line. Measurement planes are located at a) x/L = 0.2, b) x/L = 0.4, c) x/L = 0.6, d) x/L = 0.8 and e) x/L = 1.0.

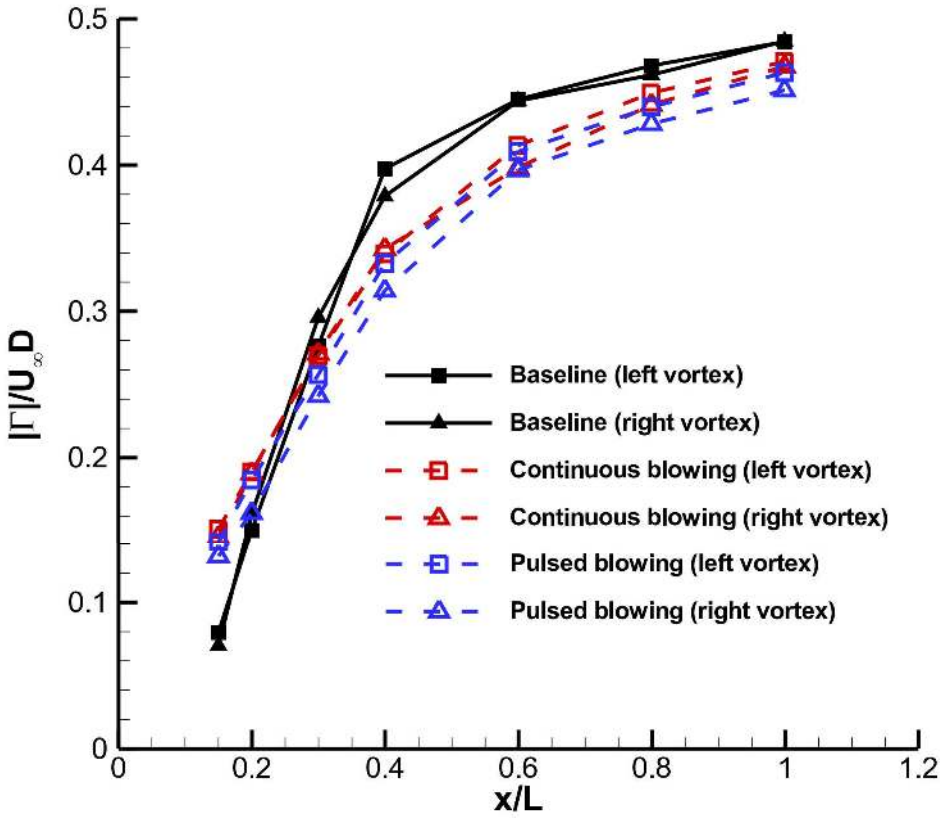

Figure 17. Development of the time-averaged crossflow vortex circulation with streamwise distance for the baseline case, continuous blowing ($\bar{C}_\mu$ = 0.0125, f = 0) and pulsed blowing cases ($\bar{C}_\mu$ = 0.0125, fD/U_∞ = 0.62).

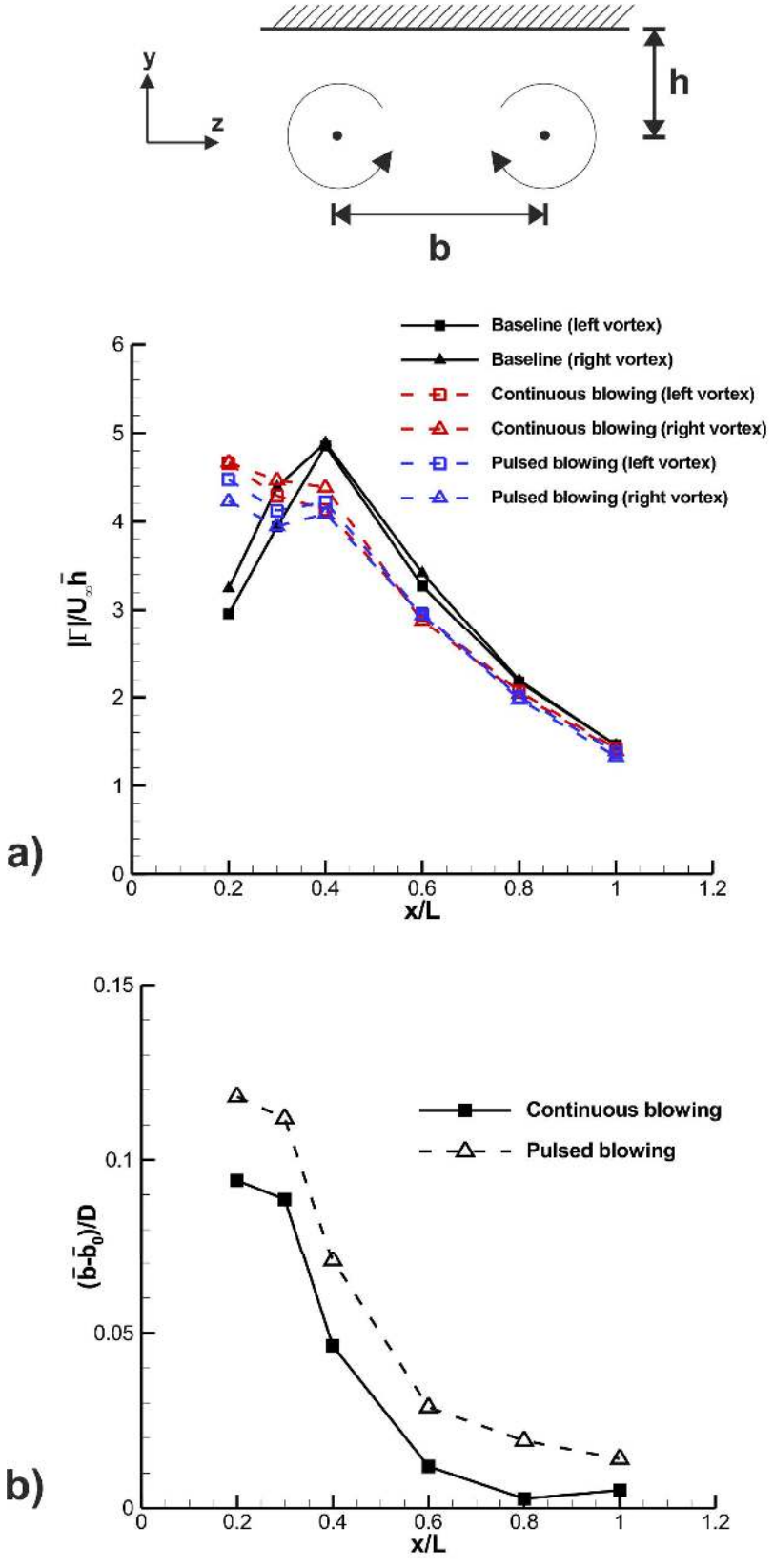

Figure 18. (a) Relative vortex strength for the continuous blowing ($\bar{C}_\mu$ = 0.0125, f = 0), pulsed blowing case ($\bar{C}_\mu$ = 0.0125, fD/U_∞ = 0.62), and the baseline, (b) spanwise vortex separation relative to the baseline case (subscript 0).

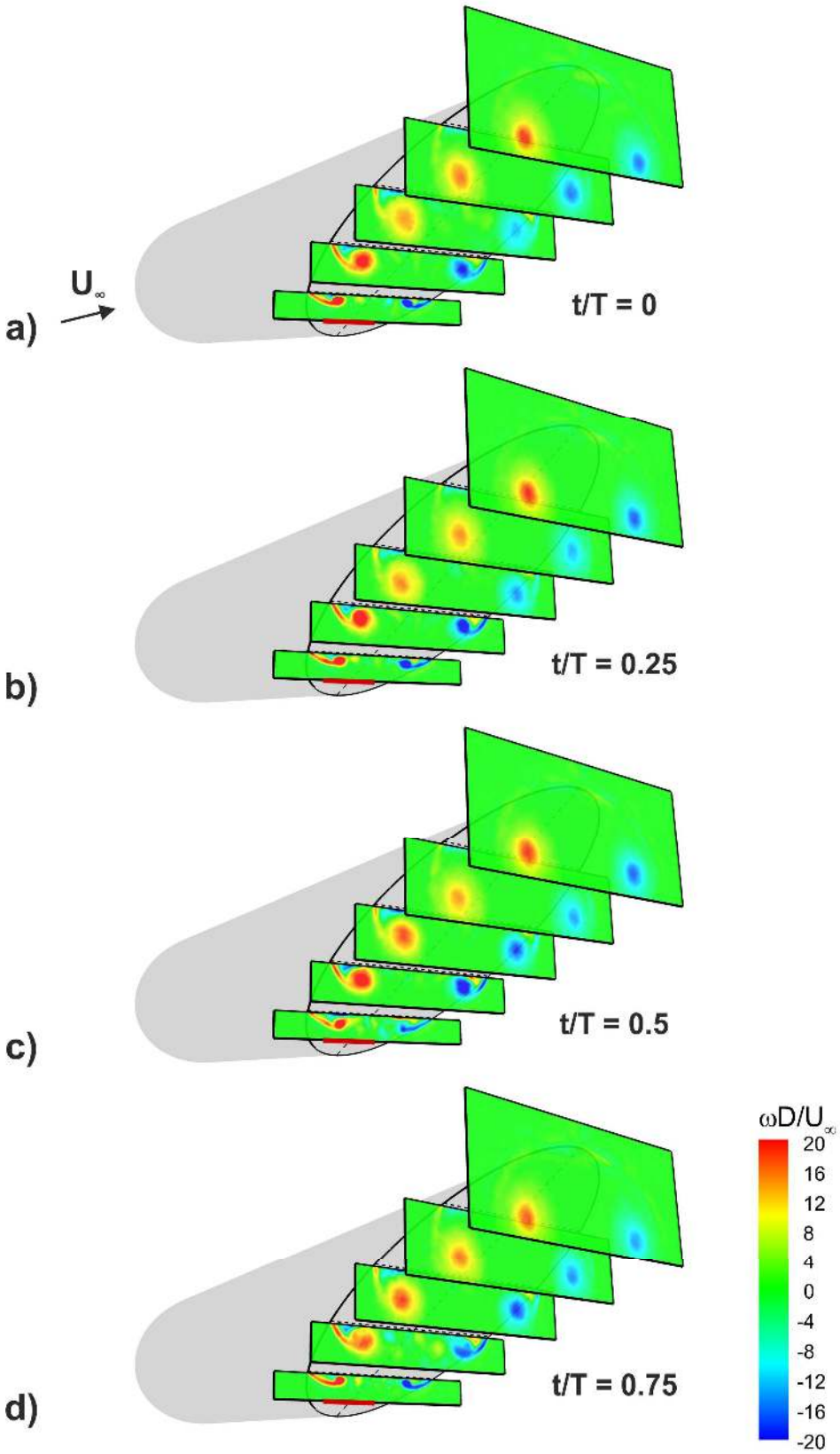

Figure 19. Phase-averaged crossflow vorticity of the pulsed blowing case ($\bar{C}_\mu$ = 0.0125, fD/U_∞ = 0.62) when a) t/T = 0, b) t/T = 0.25, c) t/T = 0.5 and d) t/T = 0.75. The location of the jet flap is marked by a red line.

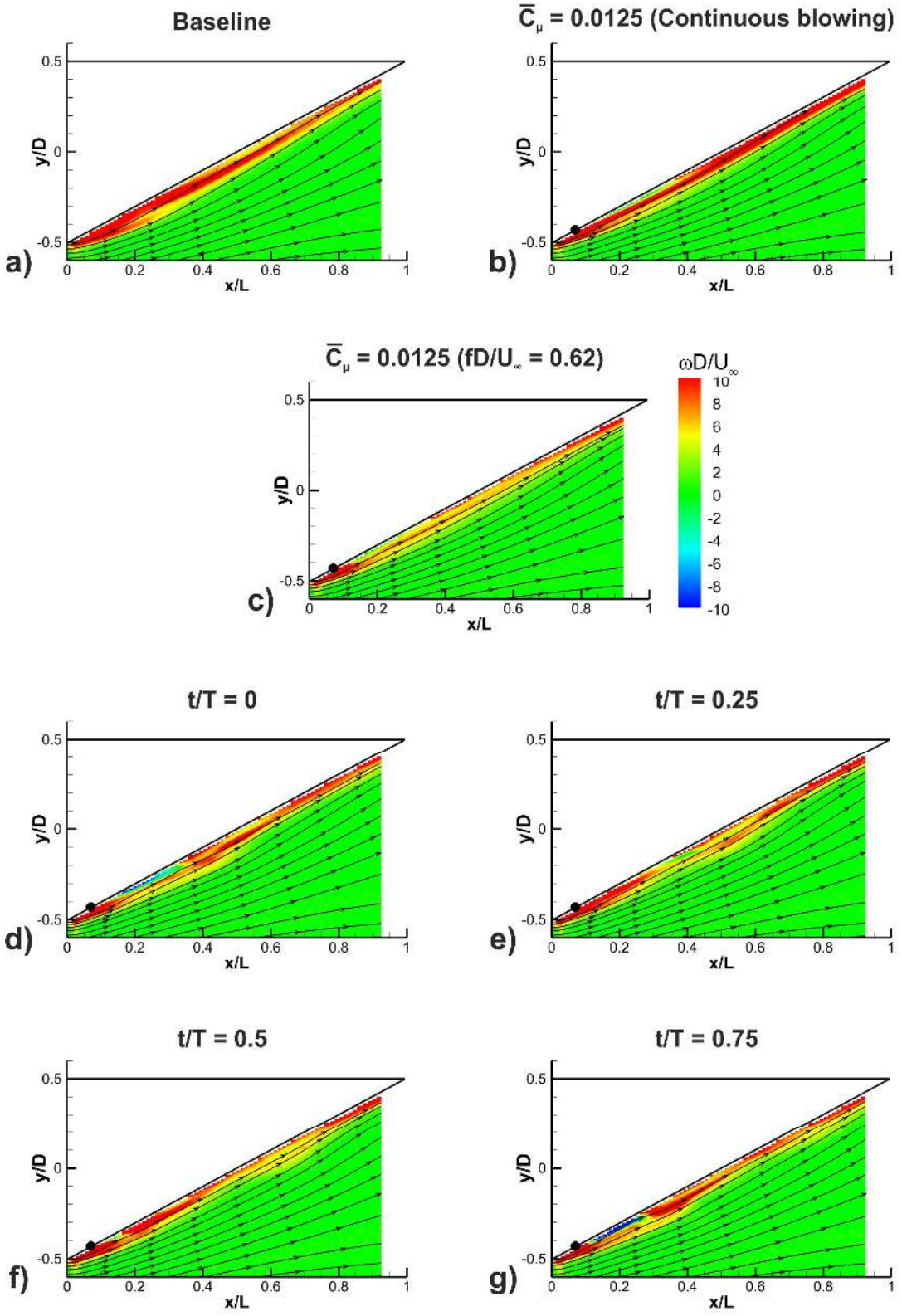

Figure 20. Vorticity and streamlines at z = 0, showing time-averaged vorticity for a) the baseline case, b) the continuous blowing case ($\overline{C}_\mu$ = 0.0125, f = 0) and c) the pulsed blowing case ($\overline{C}_\mu$ = 0.0125, fD/U$_\infty$ = 0.62). Phase-locked vorticity for the pulsed blowing case is shown in d) – g). The location of the jet is shown in b) - g) by a filled black circle.

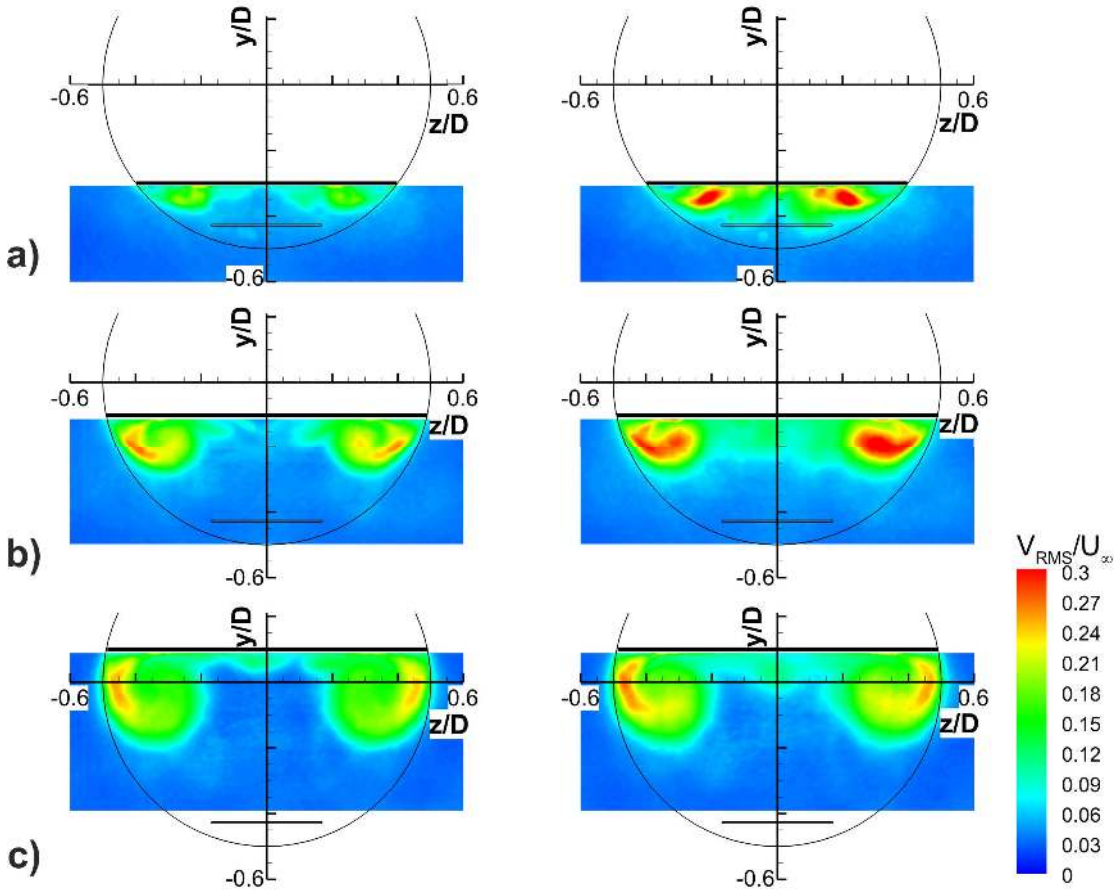

Figure 21. Crossflow RMS velocity of the continuous blowing case ($\bar{C}_\mu$ = 0.0125, f = 0), left, and the pulsed blowing case ($\bar{C}_\mu$ = 0.0125, fD/U_∞ = 0.62), right. The jet flap is marked by a black line. Measurement planes are located at a) x/L = 0.2, b) x/L = 0.4 and c) x/L = 0.6.